

Dynamical Features of Antarctic Sudden Stratospheric Warmings and Their Influences on Ozone Hole Changes

刘, 光宇

<https://hdl.handle.net/2324/4474942>

出版情報 : Kyushu University, 2020, 博士 (理学), 課程博士
バージョン :
権利関係 :

2020年度 博士学位論文

**Dynamical Features of Antarctic Sudden Stratospheric
Warmings and Their Influences on Ozone Hole Changes**

Department of Earth and Planetary Sciences
Graduate School of Science
Kyushu University

九州大学大学院 理学府 地球惑星科学専攻

大気流体力学分野

LIU GUANGYU

刘 光宇

February 2021

Abstract

Temperatures are usually very low in the austral winter due to there being less wave forcing, with variations in temperature possibly influencing stratospheric ozone concentrations. This thesis focuses on dynamical aspects of sudden stratospheric warming (SSW), especially the occurrence in September 2019. It also considers year-to-year variations in stratospheric ozone levels and their relationship with stratospheric warming, based on reanalysis and satellite data.

An unusual SSW was observed in the Southern Hemisphere (SH) in 1952 (Scherhag 1952). During such an event, a rapid deceleration or reversal of the westerly polar vortex and a sudden increase in temperature (by tens of degrees K) occurs over a period of a few days. Theoretical studies have noted that enhanced quasi-stationary planetary waves propagate upward from the troposphere to cause an SSW event (Matsuno 1971). Reversals of the meridional temperature gradient between latitudes of 90°S and 60°S and zonal-mean zonal winds at 10 hPa and 60°S may result in major or minor SSW events (Julian 1967; Labitzke 1968). SSW events are common in the Northern Hemisphere (NH) but rarely occur in the SH due to its geography, topography, and land–sea temperature contrast.

The unusual SH SSW event of September 2019 (hereinafter referred to as SSW2019) was studied using Japanese 55-year Reanalysis (JRA-55) data, which indicate a temperature reversal over 90°S–60°S and decelerated 10 hPa westerly winds at 60°S.

As reversal of the 10 hPa westerly winds was not observed at 60°S, SSW2019 is classified as a minor warming event.

Detailed analysis of SSW2019 reveals remarkable development of quasi-stationary planetary waves of zonal wavenumber 1 that caused a disturbance of the polar vortex. The strong vertical component of the Eliassen–Palm flux with zonal wavenumber 1 propagated into the stratosphere during SSW2019. Strong wave forcing occurs when zonal-mean zonal winds decelerate at high latitudes. Wave forcing in September was the strongest recorded during the 2002–2019 analysis, even stronger than that during a major SSW event in 2002. Wave propagation is controlled by the refractive index, which has positive values in the upper stratosphere at high latitudes during the warming period, implying favorable conditions for quasi-stationary planetary wave propagation upward and poleward.

The Antarctic ozone hole of 2019 and its relationship with stratospheric temperature, planetary wave evolution, and other dynamical fields were also studied. The Antarctic ozone hole undergoes major interannual changes, with that during 2017 and 2019 being at the smallest levels. Ozone profile data from the Aura Microwave Limb Sounder (MLS) were used to explain the dynamical factors that caused the small ozone hole during those years, including an investigation of daily downward motion changes and ozone transport by residual meridional circulation. It was found that intermittent surges in downward motion occurred in the mid stratosphere during the austral winter of

both years, with these causing increased downward advection of ozone-rich air, leading to smaller ozone holes.

Contents

1. INTRODUCTION	7
2. THEORETICAL BACKGROUND	10
2.1 TEM EQUATIONS	10
2.2 NON-ACCELERATION THEOREM	14
2.3 REFRACTIVE INDEX	15
2.4 SUDDEN STRATOSPHERIC WARMING	17
2.5 OZONE DYNAMICAL TRANSPORT	18
3. DATA	21
3.1 LONG-TERM REANALYSIS DATA	21
3.2 OZONE	22
4. MINOR SUDDEN STRATOSPHERIC WARMING, SEPTEMBER 2019	23
4.1 OVERVIEW OF THE AUSTRAL WINTER, 2019	23
4.2 SYNOPTIC FEATURES	26
4.3 DYNAMICAL FEATURES	31
4.4 PLANETARY WAVE PROPAGATION AND ITS EFFECT ON SSW2019	42
5. RELATIONSHIP BETWEEN THE OZONE HOLE AND DYNAMICAL PROCESSES	48
5.1 INTRODUCTION	48
5.2 ANTARCTIC OZONE HOLES IN 2017 AND 2019	53
6. CONCLUSIONS	74
ACKNOWLEDGEMENTS	78
DATA AVAILABILITY STATEMENTS	79
REFERENCES	80

SUPPLEMENTARY INFORMATION..... 89

1. Introduction

Sudden stratospheric warming (SSW) is an extraordinary event that is regularly observed in the Arctic polar region during the boreal winter, when the strong westerly jet associated with the polar vortex at middle–high latitudes decelerates and polar stratospheric temperatures increase by several tens of degrees K within a few days (e.g., Iida et al. 2014). SSW events are caused by enhanced quasi-stationary planetary waves propagating from troposphere to stratosphere. They occur more frequently in the Northern Hemisphere (NH) than in the Southern Hemisphere (SH) because of the relatively weak wave activity in the latter due to the ocean–land distribution and small wave perturbation there.

Mid-winter SSW events are classified as major or minor warming events (Julian 1967; Labitzke 1968). Major warming events involve polar vortex breakdown whereby the mean wind speed in the longitudinal direction (the “zonal-mean” zonal wind speed) poleward of 60°S reverse from westerly to easterly at the 10 hPa level with a simultaneous reversal of temperature between 60°S and the Pole. Minor warming events involve high temperatures at the Pole without reversal of 10 hPa zonal-mean zonal wind poleward of 60°S. Major warming events are classified as “vortex-displacement” or “vortex-split” types, based on the structure of the polar vortex during the warming event (Charlton and Polvani 2007). The amplification of planetary waves of zonal wavenumbers (the number

of waves in a distance 2π) 1 and 2 (PW1 and PW2) plays an important role in vortex–vortex-split events (Krüger et al. 2005).

Minor mid-winter warming events have occasionally been observed in the SH. The first recorded major SSW event occurred in 2002 (hereinafter referred to as SSW2002) (Newman and Nash 2005). Before the onset of SSW2002, a sequence of amplified planetary-wave activity was observed, which played an important role in the weakening of the polar night jet (PNJ). The polar vortex broke down in September and split into two components. The strong eastward-traveling waves (mainly PW2) led to wave–flow interactions that weakened the PNJ with the amplified quasi-stationary waves disrupting the polar vortex, abruptly increasing the temperature. The SSW2002 event was classified as a major warming event of a vortex-split type based on criteria of Charlton and Polvani (2007). The SSW2002 event significantly impacted the interannual variation of the Antarctic ozone hole. The warm temperatures and particularly strong wave activity associated with SSW2002 reduced the depletion of Antarctic ozone, leading to the smallest ozone hole recorded since 1988 (Stolarski et al. 2005).

A later SH SSW event occurred in September 2019 (Lim et al. 2020), classified as minor on the basis of Modern-Era Retrospective analysis for Research and Applications Version 2 (MERRA-2) reanalysis data and Aura Microwave Limb Sounder (MLS) data (Yamazaki et al. 2020). Rao et al. (2020) investigated the predictability of the occurrence of SSW2019 on the basis of sub-seasonal to seasonal models and described favorable

conditions that might have caused the event. Changes in zonal winds in the mesosphere over the polar region during SSW2019 were investigated using Meteor Radar and MERRA-2 reanalysis data (Eswaraiah et al., 2020). A significant reduction in ozone hole area was observed during the peak ozone depletion period as a result of SSW2019, based on analysis of Aura MLS data and Global Earth Observing System model simulation (Wargan et al. 2020). These analyses indicated that the total ozone poleward of 45°S increased during September–November 2019, as supported by Infrared Atmospheric Sounding Interferometer (IASI) data (Safieddine et al. 2020).

This thesis comprises two main parts including (1) an investigation of features and mechanisms of SSW2019 compared with SSW2002, and (2) analysis of ozone variations in the SH during SSW2019 in relation to dynamical transport.

2. Theoretical background

Here we focus on stratospheric dynamics, for the region extending from tropopause to stratopause at about the 1 hPa level (~ 50 km altitude). The stratosphere and the region above it, up to 80–90 km altitude (i.e., the mesosphere) is generally termed the “middle atmosphere”. While temperature decreases with increasing height in the troposphere, it increases with height in the stratosphere because of the existence of the ozone layer.

Useful equations and theories describing the relevant dynamical processes are described as follows.

2.1 TEM equations

Quasi-geostrophic transformed Eulerian-mean (TEM) equations (Andrews et al. 1987), Quasi-Geostrophic flow, and Eulerian means are described here.

The geostrophic balance describes the balance between Coriolis forces and horizontal pressure–gradient forces. Quasi-geostrophic flow was introduced to investigate the time development of large-scale, low-frequency geostrophic flow at mid-latitudes.

It is helpful to interpret many mid-atmospheric phenomena through the interaction of mean flow and disturbance (“wave” or “eddy”) in terms of zonal-mean and disturbance factors, respectively. For example, for wind in the longitudinal direction $u(\lambda, \phi, z, t)$, the mean flow is represented by the zonal mean of the $u(\lambda, \phi, z, t)$, denoted by an overbar:

$$\bar{u}(\phi, z, t) = (2\pi)^{-1} \int_0^{2\pi} u(\lambda, \phi, z, t) d\lambda$$

The mean definition above is an example of a Eulerian mean. A disturbance is represented by departure from the zonal mean, denoted by a prime:

$$u'(\lambda, \phi, z, t) = u(\lambda, \phi, z, t) - \bar{u}(\phi, z, t)$$

with the contribution of mean vertical velocity to adiabatic temperature change being canceled in the Eulerian-mean approach. An alternative approach involves the TEM, which provides a better diagnostic of eddy forcing by considering residual circulation (Andrews and McIntyre 1976). Residual mean circulation (\bar{v}^*, \bar{w}^*) is defined as follows:

$$\bar{v}^* = \bar{v} - \frac{1}{\rho_0} \frac{\partial}{\partial z} \left(\frac{\rho_0 \overline{v' \theta'}}{\frac{\partial \bar{\theta}}{\partial z}} \right) \quad (2.1)$$

$$\bar{w}^* = \bar{w} + \frac{1}{a \cos \phi} \frac{\partial}{\partial \phi} \left(\frac{\cos \phi \overline{v' \theta'}}{\frac{\partial \bar{\theta}}{\partial z}} \right) \quad (2.2)$$

On the basis of residual circulation, the TEM equations in spherical log(pressure) coordinates are as follows:

$$\frac{\partial \bar{u}}{\partial t} - f \bar{v}^* - \bar{X} = \frac{\nabla \cdot \mathbf{F}}{\rho_0 a \cos \phi} = DF, \quad (2.3)$$

$$\frac{\partial \bar{\theta}}{\partial t} + \bar{w}^* \frac{\partial \bar{\theta}_0}{\partial z} - \bar{Q} = 0, \quad (2.4)$$

$$\frac{1}{a \cos \phi} \frac{\partial(\bar{v}^* \cos \phi)}{\partial \phi} + \frac{1}{\rho_0} \frac{\partial(\rho_0 \bar{w}^*)}{\partial z} = 0, \quad (2.5)$$

$$f \frac{\partial \bar{u}}{\partial z} + \frac{R}{aH} e^{-\frac{\kappa z}{H}} \frac{\partial \bar{\theta}}{\partial z} = 0 \quad (2.6)$$

Here \bar{u} is the zonal-mean zonal wind speed and $f = 2\Omega \sin \phi$ is the Coriolis parameter;

$\rho_0 = \rho_s e^{-\frac{z}{H}}$ is the basic density where $\rho_s \equiv p_s / RT_s$; H is scale height; ϕ is latitude;

θ is a potential temperature; and $\theta_0 = HR^{-1}e^{\frac{\kappa z}{H}}\Phi_{0z}$ is a reference potential temperature. The Earth radius, rotation rate, and gas constant for dry air are given by a , Ω , and R , respectively. \bar{X} and \bar{Q} denote the unspecified horizontal components of friction or other non-conservative mechanical forcing, and a diabatic heating term, respectively. $\kappa \equiv R/c_p$ is the ratio of the gas constant to specific heat at constant pressure; c_p is the specific heat of dry air at constant pressure.

A zonal average is denoted by an overbar, and a disturbance component is represented by departure from the zonal mean, as denoted by a prime.

\mathbf{F} in equation (2.3) is the Eliassen–Palm (E–P) flux. DF denotes divergence or convergence of E–P flux and represents wave driving. The E–P flux in spherical and log(pressure) coordinates is as follows:

$$\mathbf{F} \equiv \left[0, -\rho_0 a \cos \phi \overline{v' u'}, \frac{\rho_0 a \cos \phi \overline{f v' \theta'}}{\theta_{0z}} \right] \quad (2.7)$$

The E–P flux can be related to wave activity density A under Wentzel–Kramers–Brillouin (WKB) conditions as follows (Edmon et al. 1980):

$$\mathbf{F} = \mathbf{c}_g A \quad (2.8)$$

$$A = \frac{E}{\bar{u} - c} \quad (2.9)$$

where \mathbf{c}_g represents group velocity, and E and c are the wave energy density and phase velocity, respectively. For more information on WKBJ The E–P flux vector is proportional to the group velocity of planetary waves and represents the direction of wave energy propagation in the meridional plane.

A generalized Eliassen-Palm theorem can be defined by:

$$\frac{\partial A}{\partial t} + \nabla \cdot \mathbf{F} = D + O(\alpha^3) \quad (2.10)$$

where A is the “wave-activity density”, the time derivative of which represents wave-transience effects. The quantity D accounts for frictional and diabatic effects. $O(\alpha^3)$ represents nonlinear wave effects.

The quasi-geostrophic beta-plane E–P is are given by:

$$\mathbf{F} \equiv \left[0, -\rho_0 \overline{v' u'}, \frac{\rho_0 f_0 \overline{v' \theta'}}{\theta_{0z}} \right] \quad (2.11)$$

For further discussion of TEM equations see Andrews et al. (1987).

2.2 Non-acceleration theorem

The divergence of the Eliassen–Palm flux in (Eq. 2.11) vanishes in the case of linear, steady, conservative planetary waves with a purely zonal basic flow (Eliassen and Palm 1961):

$$\nabla \cdot \mathbf{F} = 0 \quad (2.12)$$

Together with approximate boundary conditions, a possible mean flow satisfying TEM equation is given by

$$\bar{u}_t = \bar{\theta}_t = \bar{v}^* = \bar{w}^* = 0 \quad (2.13)$$

which is known as the “non-acceleration theorem” (Charney and Drazin 1961). This constraint should be approximately satisfied by stationary waves in the stratospheric PNJ under undisturbed situations.

2.3 Refractive Index

A modified linearized quasi-geostrophic potential vorticity equation in spherical coordinates with an ageostrophic term takes the form

$$\left(\frac{\partial}{\partial t} + \frac{\bar{u}}{a \cos \phi} \frac{\partial}{\partial \lambda}\right) q'_{(M)} + a^{-1} \bar{q}_\phi v' = 0 \quad (2.14)$$

where

$$v' = (f a \cos \phi)^{-1} \Phi'_\lambda \quad (2.15)$$

$$q'_{(M)} = \frac{1}{f a^2} \left[\frac{\Phi'_{\lambda\lambda}}{\cos^2 \phi} + \frac{f^2}{\cos \phi} \left(\frac{\cos \phi}{f^2} \Phi'_\lambda \right)_\phi + \frac{f^2 a^2}{\rho_0} \left(\frac{\rho_0 \Phi'_\lambda}{N^2} \right)_z \right] \quad (2.16)$$

and

$$\bar{q}_\phi = 2\Omega \cos \phi - \left[\frac{(\bar{u} \cos \phi)_\phi}{a \cos \phi} \right]_\phi - \frac{a}{\rho_0} \left(\frac{\rho_0 f^2}{N^2} \bar{u}_z \right)_z \quad (2.17)$$

and $\bar{u}(\phi, z)$ is the basic zonal flow; λ is the longitude; and Φ' is the geopotential disturbance.

$$\Phi' = e^{\frac{z}{2H}} \text{Re} \Psi(\phi, z) e^{is\lambda} \quad (2.18)$$

where Ψ is the amplitude; and s is the zonal wave number.

The simplified vorticity equation

$$\frac{f^2}{a^2 \cos \phi} \left(\frac{\cos \phi}{f^2} \Psi_\phi \right)_\phi + \frac{f^2}{N^2} \Psi_{zz} + n_s^2 \Psi = 0 \quad (2.19)$$

is then obtained.

To assess the behavior of wave packets, the distribution of refractive index is analyzed on the basis of

$$n_0^2 = \frac{\bar{q}_\phi}{\alpha \bar{u}} - \frac{f^2}{4N^2 H^2} \quad (2.20)$$

where n_0^2 is the “squared refractive index”; \bar{q}_ϕ is the meridional gradient of mean potential vorticity; \bar{u} is horizontal basic flow; and N is the buoyancy frequency. For more details, see Andrews et al. (1987).

2.4 Sudden Stratospheric Warming

The SSW process can be understood in terms of the interaction between zonal-mean zonal winds and eddy potential vorticities. During an SSW event, planetary wave amplitudes increase rapidly with wave transience and dissipation, with the no wave-driven mean-flow acceleration for “non-acceleration theorem” being violated as introduced in Section 2.2. This may be explained by the interaction between mean flow and waves (Andrews et al. 1987). The wave activity density in the generalized Eliassen–Palm theorem (Equation 2.10) can be expressed as

$$A \equiv \frac{1}{2} \rho_0 \overline{\eta'^2} \bar{q}_y \quad (2.21)$$

where η' represents northward parcel displacement and \bar{q}_y northward mean potential vorticity gradient.

When waves are linear and conservative, Equation 2.10 becomes $\nabla \cdot \mathbf{F} = -\partial A / \partial t$. This implies a negative force per unit mass on the zonal-mean flow. In response to that, deceleration occurs in the vicinity of the area with negative $\nabla \cdot \mathbf{F}$. This deceleration is partly opposed by the induced Coriolis term with residual meridional drift ($f\bar{v}^*$), and by vertical circulation as required by continuity. A temperature increase then occurs in the polar stratosphere.

2.5 Ozone dynamical transport

The relationship between zonal mean ozone tendency and dynamic variability is given by the transformed TEM continuity equation (Andrews et al. 1987):

$$\frac{\partial \bar{\chi}}{\partial t} = -\bar{v}^* \bar{\chi}_y - \bar{w}^* \bar{\chi}_z + \nabla \cdot \bar{\vec{M}} + \bar{S} \quad (2.22)$$

where $\bar{\chi}$ is the zonal mean mixing ratio, (\bar{v}^*, \bar{w}^*) represents the mean meridional circulation, $\nabla \cdot \bar{\vec{M}}$ is an eddy transport term, and \bar{S} represents a chemical source/sink term. A schematic representation of residual circulation of the atmosphere is given in Figure 2.1. Meridional circulation of the stratosphere, “Brewer-Dobson circulation”, includes upwelling at the tropics and downwelling in the lower stratosphere at mid and high latitudes in both hemispheres, and upwelling at the tropics and downwelling at high latitudes during winter in the middle and upper stratosphere (Plumb 2002). These circulations are interpreted as being “residual mean circulation” (Andrews et al. 1987). During winter, the stratosphere is dominated by large-amplitude, planetary-scale Rossby waves propagating upward from the troposphere. These waves drive poleward flow, upwelling in the tropics and downwelling in the vortex, thus explaining the poleward flow in the winter stratosphere (Plumb 2002). Latitude–height cross sections of the zonal mean volume mixing ratios of ozone for July are shown in Figure 2.2, indicating that maximum values occur in the low-latitude stratosphere, with high winter values over the Pole. At low latitudes, stratospheric ozone is produced photochemically, but during the polar night ozone is transported by the residual mean circulation over the Pole.

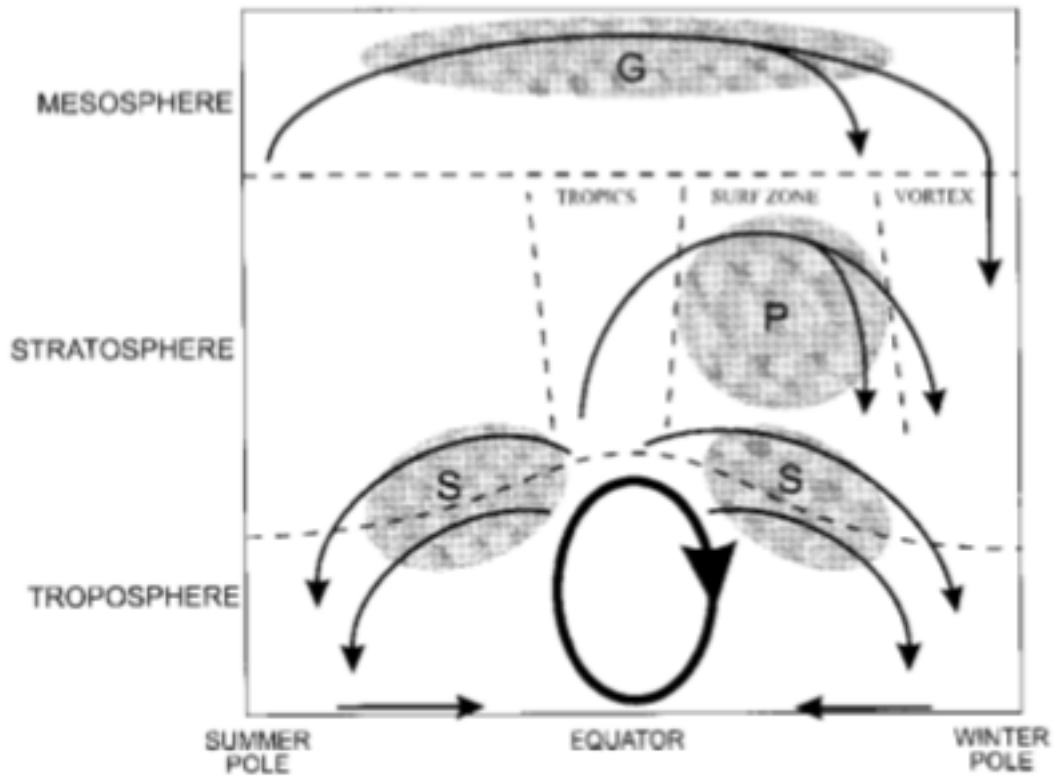


Figure 2.1. Schematic diagram illustrating residual circulation of the atmosphere. Shaded “S”, “P”, and “G” areas denote regions with breaking waves due to synoptic, planetary-scale waves, and gravity waves, respectively. (Adapted from Plumb (2002), Meteorological Society of Japan).

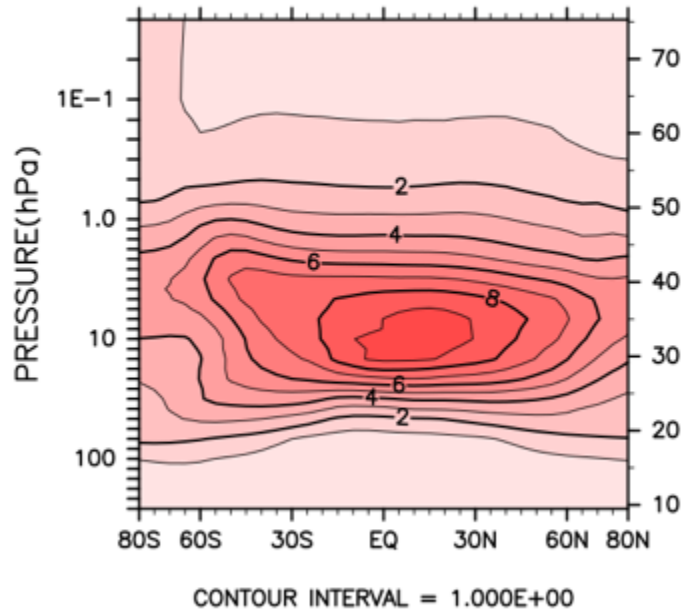


Figure 2.2. Cross section of the zonal mean volume mixing ratio of ozone (parts per million by volume, ppmv), as a function of latitude and height, for July.

3. Data

3.1 Long-term reanalysis data

In this study, zonal wind, meridional wind, temperature, and geopotential height were obtained from the Japanese 55-year Reanalysis (JRA-55) dataset provided by the Japan Meteorological Agency. JRA-55 has provided a continuous, up-to-date reanalysis dataset since 1958, with a 6-hour average temporal coverage and 1.25° longitude \times 1.25° latitude horizontal spatial coverage. In the vertical direction, the pressure-level file provides 37 pressure levels from 1000 to 1 hPa. Our analysis period was 1 June to 31 October for each year during 2002–2019, with daily data averaged from original 6-h data being used. Dataset details are provided by Kobayashi et al. (2015).

3.2 Ozone

In this study, we used stratospheric profiles of ozone volume-mixing-ratio data (version 4) obtained by the Earth Observing System (EOS) Microwave Limb Sounder (MLS) instrument and total-column ozone data from the Ozone Monitoring Instrument (OMI), with both systems being aboard the US National Aeronautics and Space Administration (NASA) Aura spacecraft platform. Aura was launched in July 2004 and has been providing data since August 2004. The spacecraft is at 705 km altitude in a sun-synchronous polar orbit, with a 13.45 (\pm 15 minutes) Equator-crossing time.

The MLS remotely measures temperature, ozone, and other constituents, providing continuous data between 82°S and 82°N, day and night, with a useful vertical range of 261–0.02 hPa. Original orbital data were gridded to 5° latitude \times 5° longitude by averaging data over three-day intervals, with data processing following the recommendations of Livesey et al. (2018). The details of the MLS instrument are provided by Water et al. (2006).

The OMI is an ultraviolet–visible nadir-viewing spectrometer that measures solar radiation backscattered by Earth’s atmosphere and surface. It measures total-column ozone with near global coverage in a single day with a spatial resolution of 13 \times 24 km. A detailed description of the instrument is provided by Levelt et al. (2006). The OMI also measures BrO, NO₂, and other trace gas concentrations in the troposphere and stratosphere (Levelt et al. 2006).

4. Minor Sudden Stratospheric Warming, September 2019

4.1 Overview of the austral winter, 2019

Figure 4.1 illustrates vertical time cross sections of the zonal-mean temperature gradients, ΔT , between 60°S and the South Pole, with a comparison of zonal-mean zonal wind speed at 60°S in 2019 and 2002. In the austral winter of 2019, regular oscillations of ΔT were evident in the upper stratosphere (5–1 hPa) from June to early July. In the SSW2002 event, intermittent warming was first observed in the upper stratosphere at the South Pole from mid-August, before the major warming in September. Except for a short warming period in the upper stratosphere in mid-August 2019, temperatures over the South Pole were lower than that at 60°S until late August. However, after two warming pulses during late August to early September, the pronounced high temperature at the South Pole began propagating downward to about 30 hPa from 19 September. The warming conditions then remained over the South Pole with regular oscillations in the mid–upper stratosphere (20–1 hPa) until late October.

Zonal-mean winds in the stratosphere were disturbed during SSW2019. From early June to late August, these winds are regularly strengthened in the mid–upper stratosphere (20–1 hPa) with two maxima in late July and late August. During the SSW2002 event, the regular oscillation of westerly winds in the mid–upper stratosphere caused a weakening of the PNJ before the zonal-mean wind reversal from westerlies to easterlies in September (Krüger et al. 2005). From late August to early September 2019,

there were two substantial weakening periods of the PNJ, from 60 m s^{-1} to $\sim 20 \text{ m s}^{-1}$ in the upper stratosphere (5–1 hPa). After considerable deceleration of the westerly winds, a reversal of zonal-mean zonal wind to easterlies occurred in mid-September above 5 hPa, before the winds reversed to weak westerlies until mid-October. Easterly winds occurred again in the upper–middle stratosphere (10–1 hPa) after mid-October, leading to a gradual transition to summer circulation. As the reversal of zonal-mean zonal winds did not occur at 10 hPa and below 60°S , SSW2019 was classified as a minor SSW event (Butler et al. 2017; Charlton and Polvani 2007).

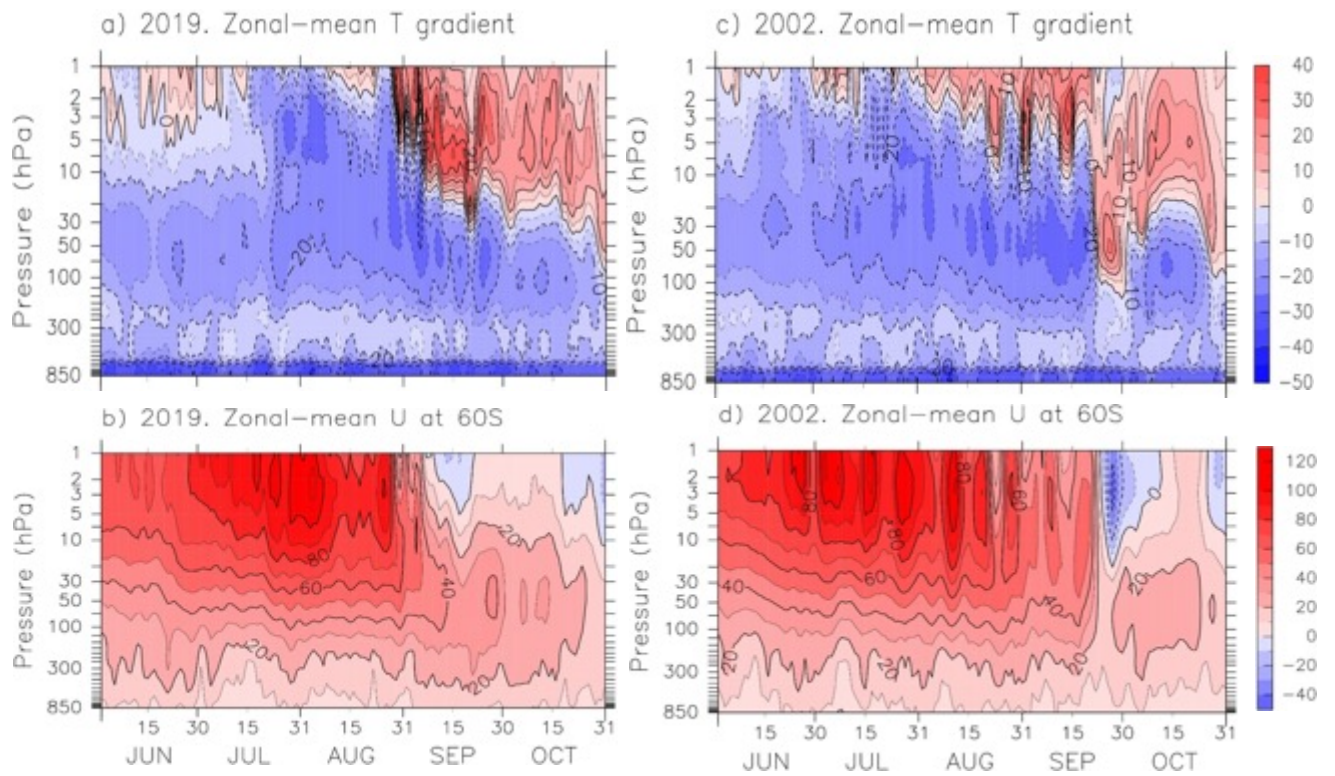


Figure 4.1. Time–altitude cross sections of the temperature gradients (ΔT , K) between 60°S and the South Pole (a, c) and zonal-mean zonal wind speed (m s^{-1}) at 60°S (b, d) for 1 June to 31 October 2019 (left) and 2002 (right). Contour intervals are 10 K for temperature and 5 m s^{-1} for zonal wind speed, respectively.

4.2 Synoptic features

The synoptic evolution of temperature and geopotential height at 10 hPa is shown in Figure 4.2 for selected days. During 25–27 August 2019, the polar vortex with low temperatures was located over the South Pole, partly surrounded by an anticyclone with warm air on its edge near South Africa. During 28 August to 2 September, the warm air became warmer and the low-temperature region began to be pushed off the South Pole. The anticyclone located to the south of Australia began to strengthen, with a corresponding amplification of planetary waves of PW1. During 3–5 September, temperatures decreased on the edge of the polar vortex, with the vortex weakening further. Centers of low temperatures were shifted off the vortex centers, indicating baroclinic conditions. During 6–8 September, the high temperature regions were elongated, almost reaching the South Pole. A pronounced warming occurred on 11 September, with a weakened cold vortex and with the anticyclone developing strongly during that period. During 12–20 September, after pronounced warming, the warm air remained over the South Pole and the anticyclone moved to the southeast of Australia.

Figure 4.3 (top) presents the daily changes of zonal-mean temperatures at 90°S and 10 hPa. The climatological temperature reached its minimum around June, with relatively little interannual variability. After that, the temperature increased gradually with increasing variability, especially for the period September to October. Temperatures in the mid stratosphere at high latitudes were higher than normal during late August to

September 2019 (red line, Figure 4.3). For comparison, the evolution of zonal-mean zonal winds in 2002, when the major SSW occurred, is shown by the green line in Figure 4.3. In 2019, the temperature was near climatological levels until mid-August when the SSW commenced. There were several episodes of warming in late August, and pronounced warming events on 31 August and 11 September 2019, with the temperature increase (ΔT) reaching $\sim 40\text{K}$ from 31 August to 11 September (referred to hereinafter as the “warming period”). A slight temperature decrease occurred after the large increase, but high temperature conditions extended beyond one more week. The temperature finally attained a peak value of $\sim 275\text{K}$ on 19 September, ~ 10 days earlier than in 2002. The magnitude of the warming peak over the South Pole in September 2019 extended well beyond plus one standard deviation of the mean.

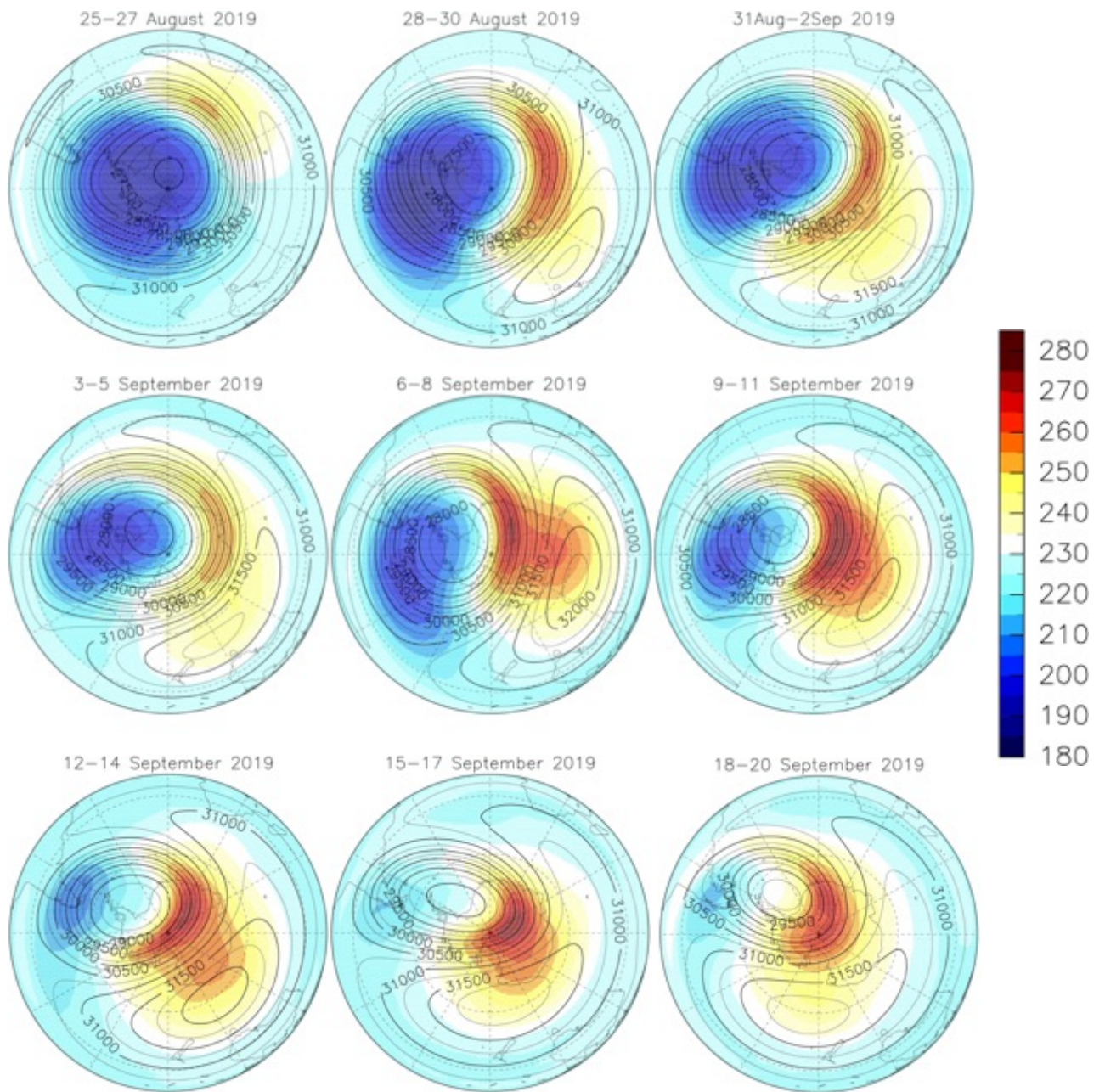


Figure 4.2. Polar stereo maps of temperatures (K, color) and geopotential heights (m, contours) in the Southern Hemisphere at 10 hPa, based on three-day averages from 25 August to 20 September, 2019. The contour interval is 250 m.

Details of changes in zonal-mean zonal winds were acquired. Figure 4.3 (bottom) displays zonal-mean zonal winds at 60°S and 10 hPa (red line) in the region near the peak of the of the PNJ maximum. Climatological values (blue line) are shown together with daily standard deviations of interannual variability (shaded region). The change during the major SSW2002 event is depicted by a green line. The climatological zonal-mean zonal wind speed peaked in August before decreasing with large interannual variability. In 2019, a pronounced deceleration of the westerly wind occurred on 31 August (to ~ 61 m s^{-1}), corresponding to the warming of late August. The westerly wind speed reached a value of ~ 26 m s^{-1} on 11 September, with a temperature warming peak. The magnitude (ΔU) of wind weakening was ~ 35 m s^{-1} with the deceleration continuing until mid-September, to ~ 11 m s^{-1} on 17 September. The wind speed decreased by ~ 50 m s^{-1} between 31 August and 17 September, 2019. In 2002, the PNJ was converted to easterly winds on 27 September (-20 m s^{-1}), contrasting with 24 August when a warming pulse occurred with wind speeds decreasing by ~ 72 m s^{-1} . Similar to the temperature changes, the zonal-mean zonal wind weakened to well below minus one standard deviation of the mean during September. However, in contrast to the major SSW of 2002, there was no zonal wind reversal in 2019.

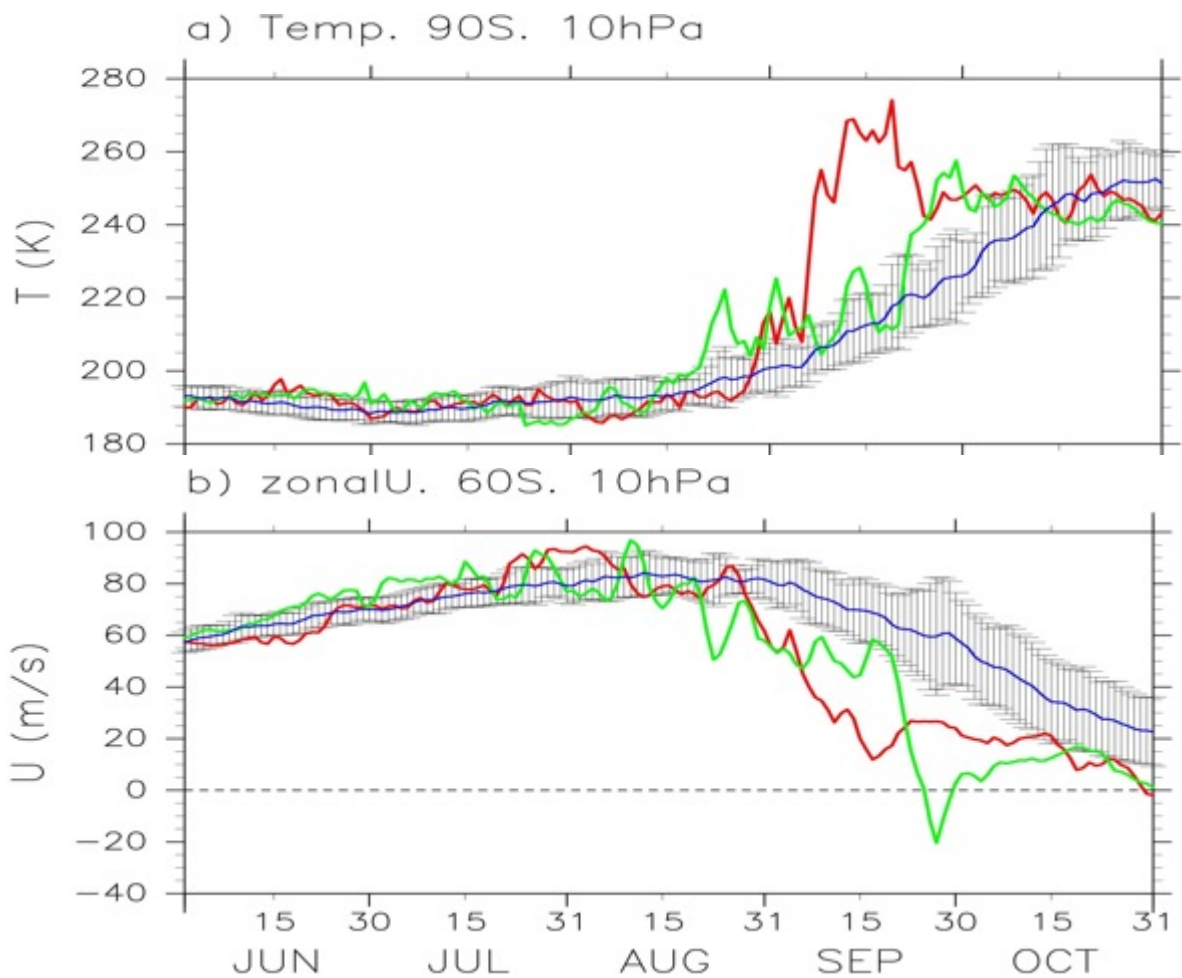


Figure 4.3. Time series of temperature (K) at 90°S , 10 hPa (a) and zonal-mean zonal wind speed (m s^{-1}) at 60°S , 10hPa (b) from 1 June to 31 October. The red and green lines indicate 2019 and 2002, respectively. Climatological values for 2002–2019 are represented by blue lines with the standard deviations as shown.

4.3 Dynamical features

Daily changes of wave amplitudes, the Fourier-analyzed geopotential heights Z of wave numbers 1 ($Z1$) and 2 ($Z2$) (the geopotential height waves of PW1 and 2), at 60°S and 10 hPa (top) and 50 hPa upward E–P fluxes of zonal PW from 1 to 3 (bottom), as defined by Equation (2.11), are shown in Figure 4.4 for 2019, with corresponding quantities in 2002 shown in the right panels for comparison.

The quasi-stationary PW1 played an important role in the dynamical evolution of the SSW2019 event. The amplitude of $Z1$ exceeded 2000 m on 8 September (~ 2137 m). Large $Z1$ amplitudes occurred from late August to mid-September, consistent with the warming period. Yamazaki et al. (2020) reported that this was the highest value for $Z1$ observed since August 2004 by the Aura MLS in the SH. Another large amplification of $Z1$ occurred in late August. These large amplifications of PW1 disturbed the polar vortex, leading to a reduction of the PNJ (Eswaraiah et al. 2020). The large increase in PW1 may be associated with the easterly phase of the quasi-biennial oscillation in the tropics (Eswaraiah et al. 2020; Rao et al. 2020). Contrasting with the dominant role of PW1, PW2, and PW3 in the major SSW2002, $Z2$ appeared less dominant during the warming period from late-August to early-September in SSW2019.

Hovmöller diagrams of geopotential height (Z) were studied to identify dominant wave modes, with diagrams for $Z1$ and $Z2$ in the SH for 2019 and 2002 at 10 hPa being shown in Figure 4.5. $Z1$ amplitudes became dominant in the stratosphere from around 10

August to 20 September 2019, while the eastward-traveling Z2 waves appeared on 31 July, 10 August, and 20 September at 10 hPa. In 2002, the Z1 amplitudes strengthened from mid-August to mid-September with Z2 waves travelling eastward from mid-July to mid-September. The Z1 and Z2 amplitudes increased alternately, becoming dominant during mid-September when the major SSW occurred (Krüger et al. 2005). However, in 2019, the Z1 amplitudes became dominant in the stratosphere during the SSW.

The vertical component of the E–P flux (EPFz hereinafter) is a useful diagnostic for evaluating the vertical propagation of planetary waves to the stratosphere (Harada and Hirooka 2017). In Fig. 4.4(b, d), the daily evolution of the total EPFz at 50 hPa for all three wavenumbers are indicated by gray shading, together with the EPFz of PW1–3 (colored lines). Upward-propagating waves originate in the troposphere and propagate into the stratosphere, so the EPFz in the lower stratosphere was used to investigate wave propagation. The total EPFz in 2019 depicts active planetary waves propagating to the stratosphere, beginning in late August and peaking in the first half of September, corresponding to increasing temperature at South Pole and weakening westerly winds. The contribution of the zonal wavenumber 1 component was considerably larger than that of other wavenumber components. However, the PW1, PW2, and PW3 components played an important role in SSW2002 (Krüger et al. 2005). Furthermore, the peak value of total EPFz did not exceed that of 2002. The SSW2019 event was characterized by a

large increase in wave activity of PW1, which disturbed the polar vortex before and during the SSW.

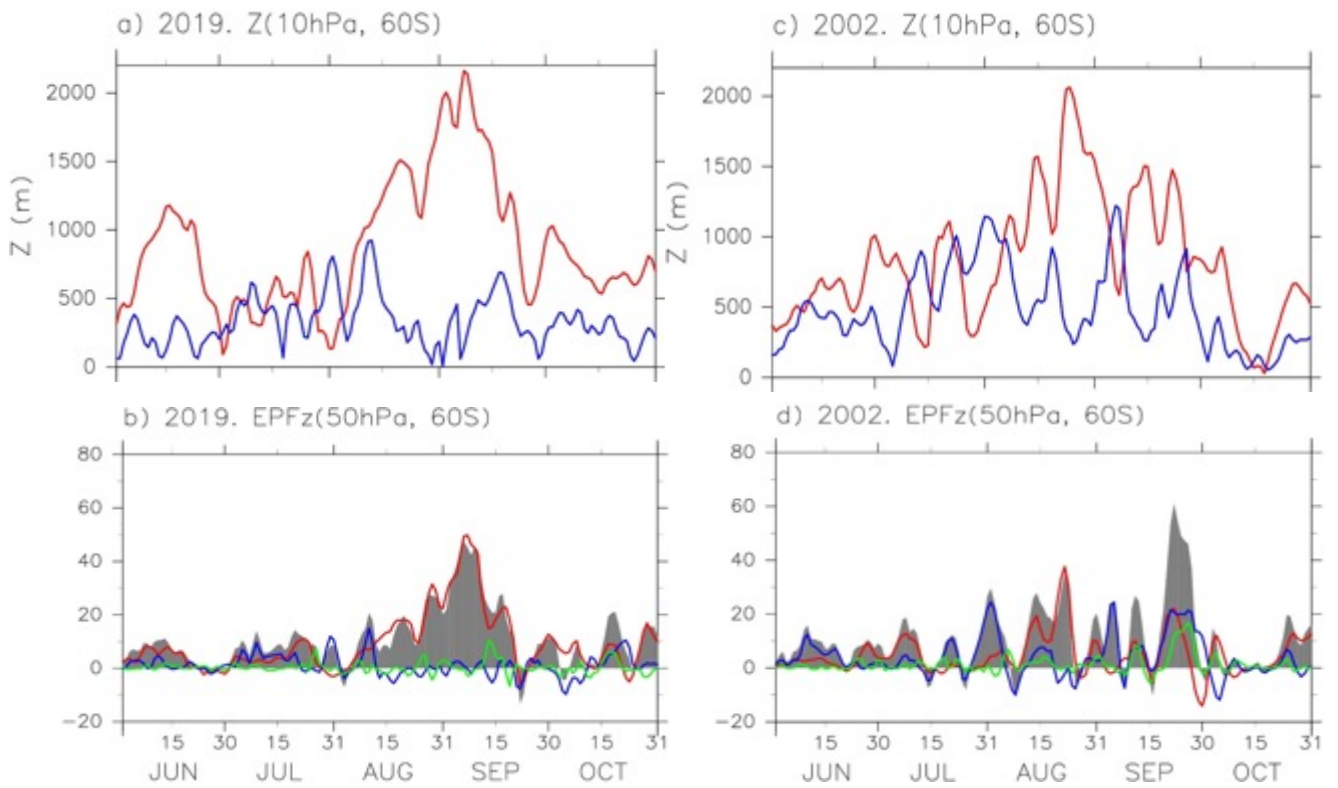


Figure 4.4. Time series of geopotential height (Z , m) at 10 hPa, 60°S, (a, c) and the vertical components of E–P flux [$\times 10^4 \text{ kg s}^{-2}$] at 50 hPa, 60°S, (b, d) for 1 June to 31 October 2019 (left) and 2002 (right). Red, blue, and green lines indicate zonal wave numbers 1, 2, and 3, respectively. Grey shading denotes the vertical components of the E–P flux for all zonal wave numbers.

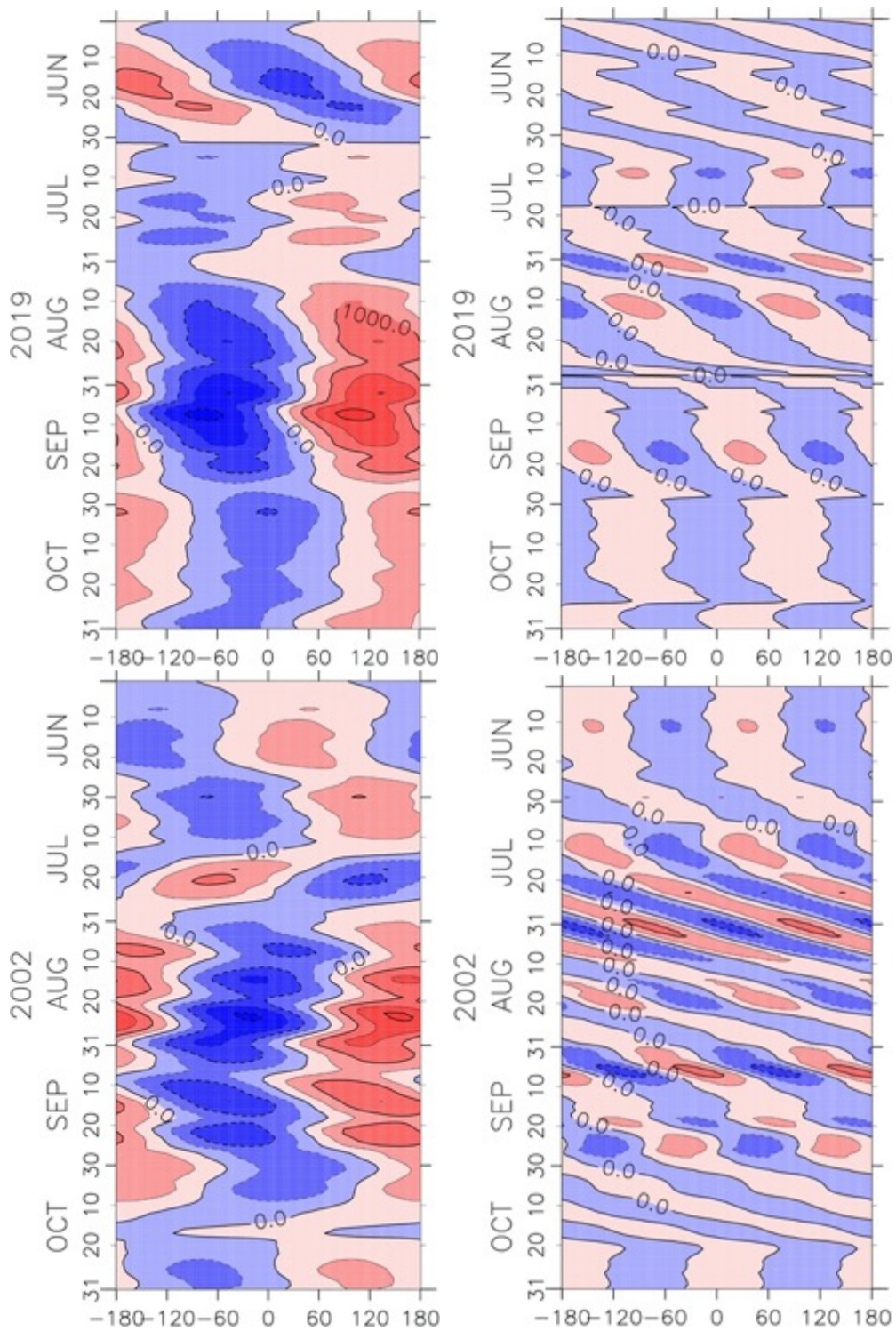


Figure 4.5. Hovmöller diagrams of planetary Z_1 (left) and Z_2 (left) at 10 hPa, 60°S, for 2019 (top) and 2002 (bottom) 2002. Contour intervals are 500 m for 10 hPa pressure levels.

Latitude–height cross sections of zonal-mean zonal winds are shown for selected days in Figure 4.6. During 25–27 August 2019, there were westerly winds in the stratosphere at high latitudes with large amplitudes and wave activities occurring from late August to early September. The PNJ strength weakened considerably during 28–30 September 2019, with the core peak wind speed decreasing to $\sim 65 \text{ m s}^{-1}$ from $>90 \text{ m s}^{-1}$ during 25–27 August 2019. Due to the high wave activity after late August, a substantial deceleration of PNJ was observed during the period 28 August 2019 to 2 September 2019. After slight strengthening of PNJ during 3–5 September 2019, the PNJ weakened with its core propagating downward during 6–11 September 2019, corresponding to the large temperature increase (Figure 4.2). After the substantial deceleration of the PNJ, westerly winds remained relatively weak during 12–20 September 2019 and were characterized by a poleward shift of the westerly jet axis below 10 hPa. The deceleration of the PNJ during 12–20 September 2019 corresponded to warming over the South Pole (Figure 4.2).

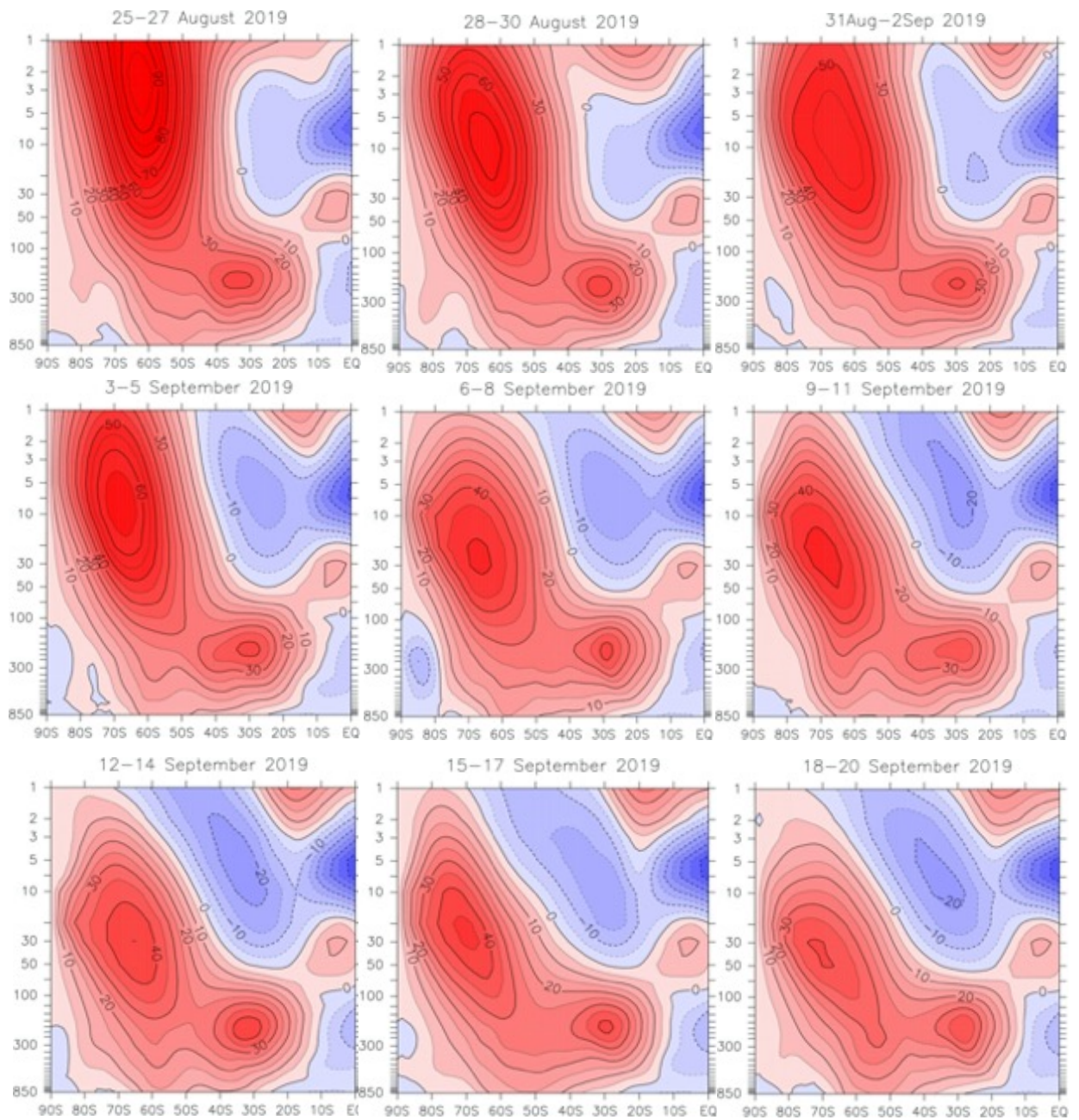


Figure 4.6. Latitude–height cross sections of zonal-mean wind speed (m s^{-1} ; three-day averages) for 25 August to 20 September 2019. The contour intervals are 5 m s^{-1} .

The development of wave propagation from troposphere to stratosphere was considered by examination of the E–P flux. Time–height cross sections of E–P flux vectors and the divergence for PW1 and 2 at 60°S are shown in Figure 4.7. In the case of PW1 for SSW2019, there was a large upward propagation from troposphere to stratosphere and strong convergence of the E–P flux in the upper stratosphere in late August and early September (Figure 4.7a). In contrast to the large wave activities of PW1, those of PW2 were fairly weak during that period (Figure 4.7b). This suggests that the strong upward-propagating PW1 waves and the strong convergence played an important role in the occurrence of SSW2019.

Planetary wave activity during the SSW2002 event was well documented (Baldwin et al. 2003). Regular strengthening of planetary waves from troposphere to stratosphere for both PW1 and 2 are shown in Figure 4.7c, d. Strong convergence of the E–P flux appeared intermittently in the upper stratosphere for both PW 1 and 2, indicating that the PNJ was weakened in 2002 by the intermittently strong wave activities prior to the SSW, pre-conditioning, and the weakened polar vortex. As a result, the polar vortex was broken down by large wave activity in late September, with reversal of zonal winds at 60°S, 10 hPa (Figure 4.3b).

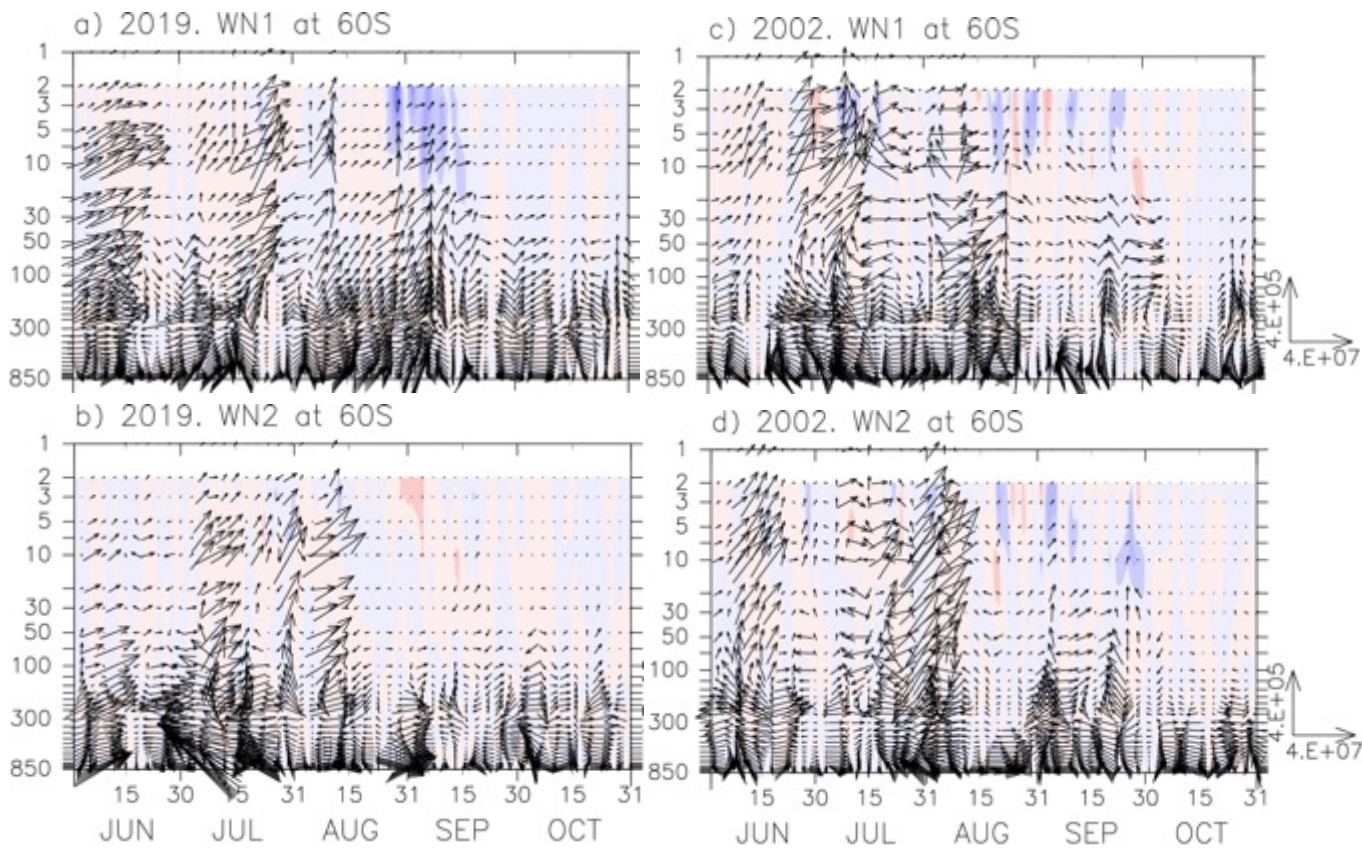


Figure 4.7. Time–height cross sections of the E–P flux vectors (kg s^{-2}) at 60°S for wavenumber 1 (a, c) and 2 (b, d), and divergence (shading) from 1 June to 31 October in 2019 (left) and 2002 (right). The right-ward direction of the horizontal component vector indicates pole-ward movement. Blue and red shading denotes convergence and divergence of the E–P flux, respectively.

Figure 4.8 shows meridional cross sections of E–P flux vectors (\mathbf{F}) and wave driving (divergence/convergence of E–P flux; DF) related to the acceleration/deceleration of zonal-mean zonal winds for the days shown in Figure 4.6, where \mathbf{F} and DF are the terms defined in the TEM equation (Eq. 2.3). Wave transience would result in E–P flux convergence or divergence, leading to westerly wind deceleration or acceleration (Andrews et al. 1978). Pulses of strong wave-forcing occurred in the stratosphere at high latitudes from late August to early September, 2019.

During 28–30 August 2019, the waves were propagating strongly upward and poleward at 60°S. Strong convergence occurred in the upper stratosphere, corresponding to the highly amplified waves and leading to deceleration of the PNJ. The waves propagated upward and Equator-ward, with E–P flux convergence occurring in the upper stratosphere extra-tropically during 31 August to 5 September 2019. During 6–8 September 2019, a second maximum of E–P flux convergence occurred with upward wave propagation from troposphere to upper stratosphere at around 60°S. This contributed to the occurrence of SSW2019 through deceleration of the PNJ and warming over the polar ice-cap. After the considerably high wave activity, E–P flux convergence persisted at high latitudes at around 10 hPa until 20 September 2019, corresponding to the continuous warming and weakening of the PNJ as seen in Figures 4.2 and 4.6.

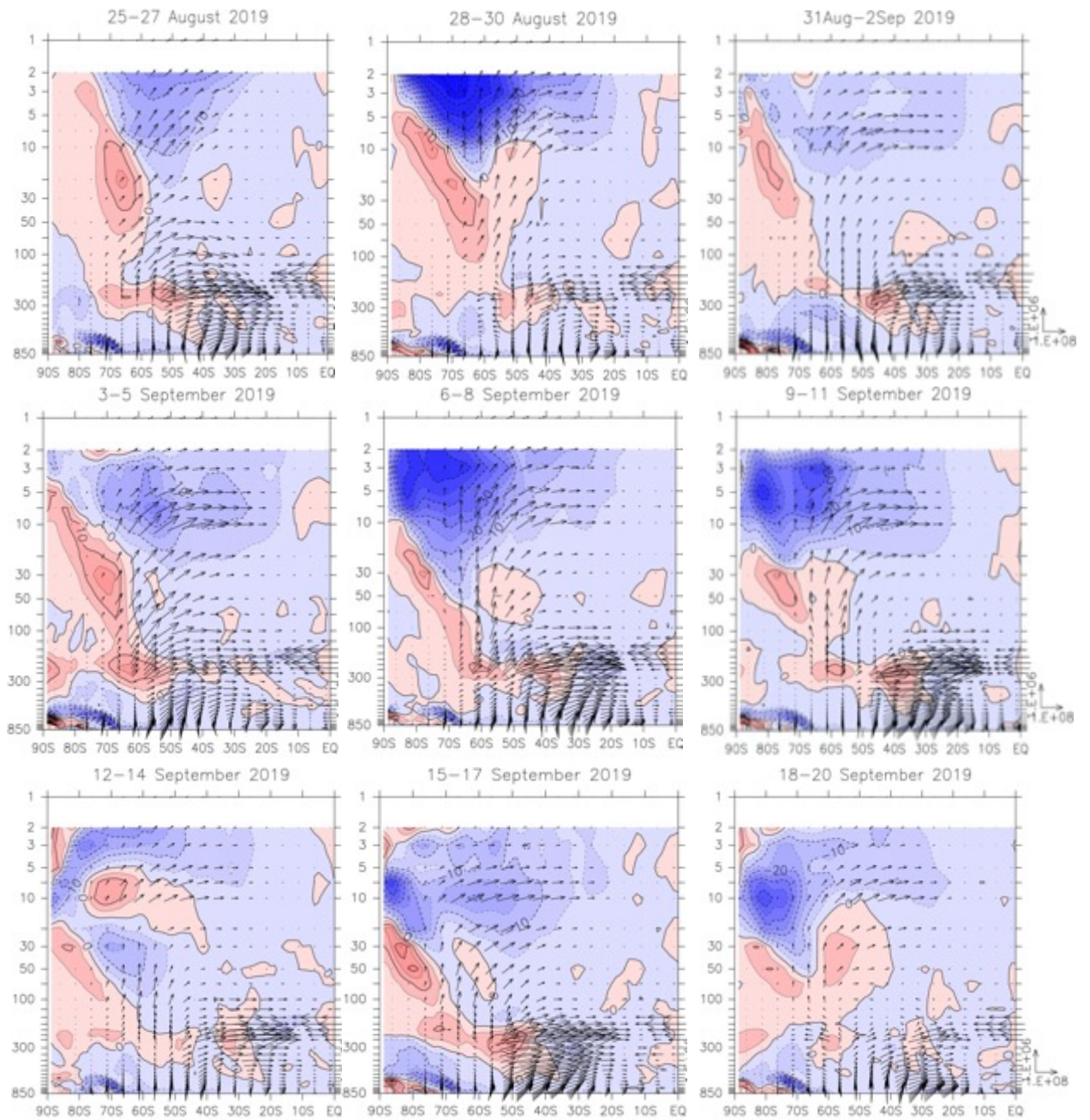


Figure 4.8. Divergence of the E-P flux (color contours, $\text{m s}^{-1} \text{ day}^{-1}$) as for Figure 4.6.

4.4 Planetary wave propagation and its effect on SSW2019

In September 2019, the polar vortex was weakened by strong PW1 forcing (Figures 4.2 and 4.4). Wave–flow interaction with acceleration or deceleration of zonal flow was considered in terms of divergence/convergence of the E–P flux. The interannual variation of divergence/convergence of the E–P flux with WN1 and 2 components in September for 30°S–90°S at 10 hPa, for 2002–2019, is shown in Figure 4.9. Convergence of the E–P flux in 2019 was the highest of the past 18 years, and its divergence for PW1 was the highest in 2019 (Figure 4.9). However, apart from 2019, the E–P flux divergence in 2002 was the second lowest during the analysis period. The PW1 and PW2 components thus played an important role in SSW2002, consistent with results of Krüger et al. (2005).

A striking difference between the unusual major SSW2002 and minor SSW2019 events in the SH is that the zonal-mean zonal winds did not reverse in 2019. Preconditioning is considered a characteristic of major SSW events (Labitzke 1981) with many studies having demonstrated its importance in SSW2002 (Allen et al. 2003; Baldwin et al. 2003; Newman and Nash 2005). Krüger et al. (2005) highlighted the importance of the interaction of the eastward-traveling PW2 with the quasi-stationary PW1, which weakened the PNJ prior to the major SSW events. For SSW2019, the planetary wave activity was not large (amplified) until late August. Furthermore, compared with that in 2002, the eastward-traveling PW2 was less active and pronounced before SSW2019 (Figure 4.5). The September SSW2019 event occurred when the PNJ

still had strong westerly wind conditions, but the wind speed decreased to $\sim 50 \text{ m s}^{-1}$ from late August to early September (Figure 4.3). The strong divergence of the E–P flux did not result in reversal of zonal winds at 10 hPa (Figure 4.3). However, similar or even smaller magnitudes of deceleration may result in reversal of zonal winds, as observed for the major NH SSW in winter of 2018/2019 (Rao et al. 2020). The weakening of westerly winds by $\sim 50 \text{ m s}^{-1}$ at 60°N , 10 hPa, may lead to a major NH SSW (Wargan et al. 2020).

The sudden occurrence of wave propagation in the stratosphere also played an important role in the occurrence of SSW2019. As mentioned in Section 4.3, strong upward planetary wave propagation occurred from late August to early September 2019. A possible mechanism for wave propagation to the stratosphere involves the refractive index and meridional potential vorticity being strongly correlated in the SH near the tropopause, and with wave propagation from troposphere to stratosphere being controlled by the refractive index (Dickinson 1968; Newman and Nash 2005).

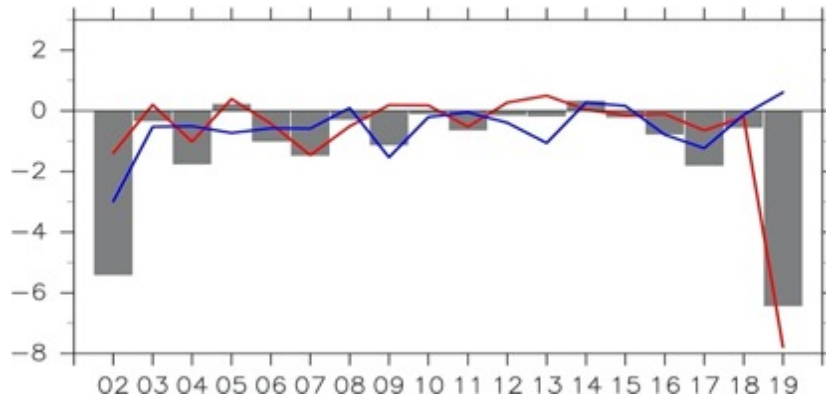


Figure 4.9. Interannual variation of the divergence of E–P flux ($\text{m s}^{-1} \text{ day}^{-1}$) at 10 hPa averaged over 30°S – 90°S in September for WN 1 (red line) and WN 2 (blue line), 2002–2019. All wave numbers are indicated by the gray bars.

Meridional cross sections of the squared refractive index (n_0^2), as defined in Section 2.3, before, during, and after SSW2019 are shown in Figure 4.10. From 28 August to 11 September (during the SSW), a wide waveguide (positive refractive index) occurred from troposphere to stratosphere at around 60°S. Planetary waves were able to propagate upward to the stratosphere through this waveguide, consistent with strong wave propagation during the warming period (Figure 4.8). The waveguide persisted at high latitudes until 20 September, with its duration allowing wave-energy propagation from troposphere to stratosphere possibly with weakening of the PNJ. Furthermore, the waveguide propagated downward at high latitudes during the period 12 September to 20 September (after the SSW). Planetary wave packets propagate mainly in regions with a large positive squared refractive index (n_0^2) value with no propagation in negative-value regions. During the period 28 August to 11 September, refractive index values were high at high latitudes and up to ~5 hPa. Westerly wind speed reduced to ~55 m s⁻¹ at ~65°S and 10 hPa, suggesting that planetary waves may propagate in moderate environments from the upper troposphere at up to ~5 hPa (Naoe et al., 2020). During this period, strong upward-propagating planetary waves and convergence of the E–P flux occurred at about 65°S and 10 hPa (Figure 4.8). An open waveguide persisted during 12–20 September at high latitudes after the pronounced warming in early September. This suggests that the existence of an open waveguide allows planetary-wave propagation from troposphere to

stratosphere, with downward propagation of core westerly winds occurring when the waveguide and E-P flux convergence extend below about 30 hPa.

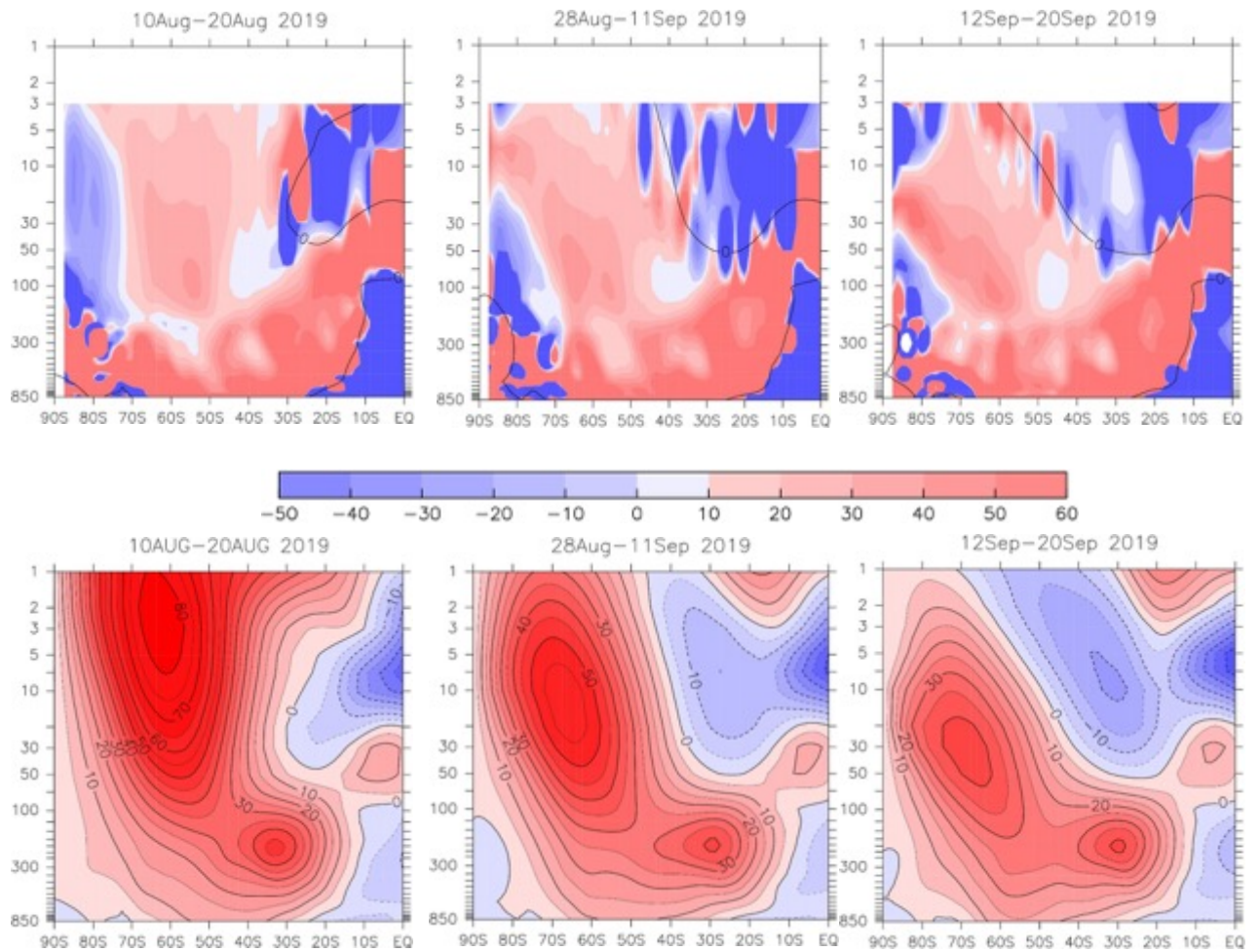


Figure 4.10. Same as Figure 4.5, but for the quasi-geostrophic refractive index (shading, top) and zonal wind (bottom), averaged over 10–20 August (left), 28 August–11 September (middle), and 12–20 September (right) in 2019. Black lines in the top panels denote wind 0 m s^{-1} wind speed.

5. Relationship between the ozone hole and dynamical processes

5.1 Introduction

The extreme ozone depletion phenomenon occurs during the austral spring in the lower stratosphere over Antarctica. The resulting Antarctic ozone hole has been observed since the late 1970s (Chubachi 1984; Farman et al. 1985; Komhyr et al. 1986; Solomon 1999; Stolarski et al. 1986). Current understanding of the Antarctic ozone hole involves mainly photochemical O₃ destruction by catalytic cycles involving Cl- and Br-bearing compounds, with meteorological conditions promoting their transport to the stratosphere.

Severe ozone depletion in the austral spring in the Antarctic is understood to be a result of the chlorine catalytic cycle with heterogeneous depletion reactions occurring in polar stratospheric clouds (PSCs) that form only at extremely low temperatures (Solomon 1999). Chlorine compounds are converted from reservoir species such as HCl and ClONO₂ to more reactive species such as Cl₂ and HOCl (Brasseur and Solomon 2005). Because there is less planetary wave activity in the SH, the polar vortices are stable and temperatures are usually low enough to form PSCs during the austral winter. The ozone hole has therefore formed in the SH during every austral winter since its discovery.

Some studies have suggested a decrease in atmospheric chlorine levels may prevent ozone depletion (Salby et al. 2012). The evolution of atmospheric concentrations of selected chlorofluorocarbons (CFC-11, CFC-12 and CFC-13) in the SH are shown in Figure 5.1, indicating the decrease in CFC levels resulting from the Montreal Protocol

regulations (Solomon et al. 2016). However, chlorine and bromine levels in the stratosphere are still high enough to cause severe ozone depletion. For example, even though the 2012 ozone hole was the second-smallest observed since 1988, depletion was still evident during August and early September due to chlorine reactions in the ozone hole area (Kramarova et al. 2014). This indicates the influence of wave dynamics on the ozone hole and its influence on stratospheric temperatures (Weber et al. 2003). Transport of ozone from the tropics to middle–high latitudes involves the meridional Brewer–Dobson circulation (Section 2). In the stratospheric winter, propagation of planetary waves into the stratosphere leads to upwelling at tropical latitudes and downwelling at middle–high latitudes.

The ozone hole area, which is defined as the region with total-column ozone values of <220 Dobson units (one Dobson unit (DU) corresponds to a column ozone thickness of $10 \mu\text{m}$ at 273K and 1 atmosphere pressure.) and is located south of 40°S , is a primary metric for assessing the severity of Antarctic ozone depletion. The 220 DU level was chosen as being lower than levels applying before occurrence of the ozone hole (Newman et al. 2004). Annual variations in the SH maximum daily ozone-hole area, 1979–2020, are illustrated in Figure 5.2., based on NASA data. The Antarctic ozone hole expanded rapidly from the 1980s to the mid 1990s, with a decreasing trend in the hole area thereafter with signs of recovery of springtime Antarctic ozone levels (Solomon et al. 2016).

The interannual variability of the Antarctic ozone hole is associated with dynamic changes. Weber et al. (2003) demonstrated a strong correlation between wave activity at high latitudes and high-latitude total-ozone levels, with increased wave activity being associated with higher total-ozone levels. For example, in 2002 an anomalously small ozone hole (area $\sim 2.2 \times 10^7 \text{ km}^2$) was observed coincident with major SSW events in the SH in September, with anomalously high temperatures and a disrupted polar vortex resulting from strong wave activities (Krüger et al. 2005). The higher temperatures prevented formation of PSCs, limiting ozone loss (Allen et al. 2003; Baldwin et al. 2003; Newman and Nash 2005). Furthermore, in 2012 a small ozone-hole area of $2.1 \times 10^7 \text{ km}^2$ was observed as one of the smallest since the 1990s (Kramarova et al. 2014). The hole area ($\sim 1.96 \times 10^7 \text{ km}^2$) in spring 2017 was at the level of the 1980s (Evtushevsky et al. 2019). During 2019, when a minor SSW event occurred (Section 4), the maximum daily ozone hole area ($1.64 \times 10^7 \text{ km}^2$) was smaller than that in 2017.

We compared ozone-hole area data provided by the JMA with that provided by NASA. The JMA defines the hole area as the region with ozone levels of $<220 \text{ DU}$ south of 45°S , with the different definition resulting in different hole areas. For example, the JMA maximum daily ozone hole areas for 1988, 2002, 2017, and 2019 were $\sim 1.37 \times 10^7$, $\sim 2.17 \times 10^7$, $\sim 1.91 \times 10^7$, and $\sim 1.37 \times 10^7 \text{ km}^2$, respectively (Figure 1S). JMA data indicate that in 2019 the ozone hole was as small as that in 1988, and smaller than that provided by NASA.

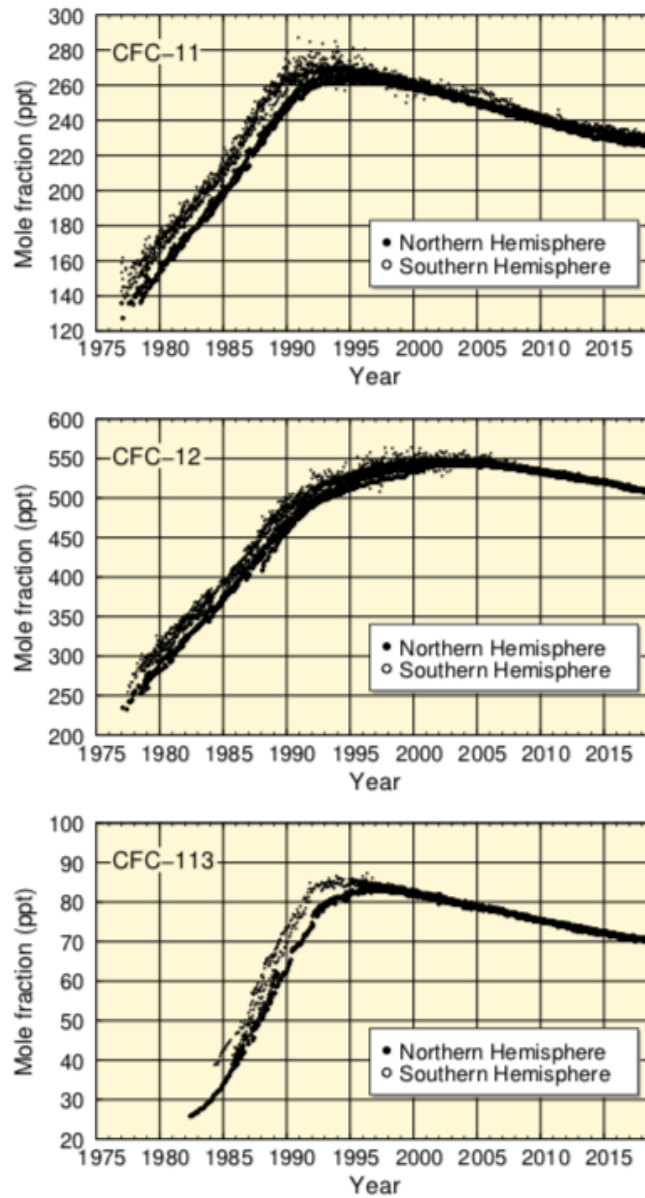


Figure 5.1 Time series of the monthly mean atmospheric mole fractions of CFC-11, CFC-12 and CFC-113. After WMO WDCGG (2020).

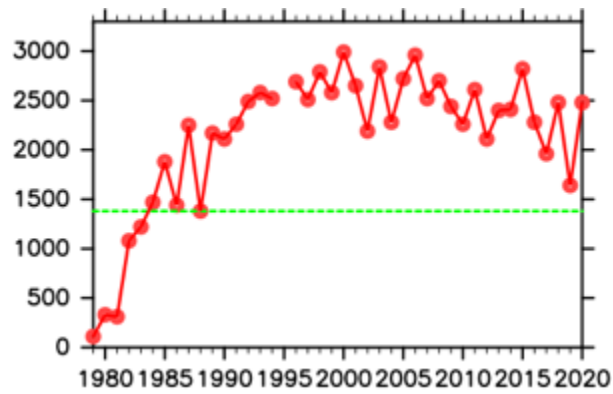


Figure 5.2 Time series of SH maximum of the daily ozone hole area ($\times 10^4 \text{ km}^2$) based on data from the NASA Total Ozone Mapping Spectrometer, OMI, and Ozone Mapping Profiler Suite data, 1979–2020. There were no data for 1995. Green line indicates the 1988 value.

5.2 Antarctic ozone holes in 2017 and 2019

The years 2017 and 2019 are interesting cases for which to explore relationships between the ozone hole and dynamical effects. In 2019, there was an anomalously small ozone hole in the SH (Wargan et al. 2020). Although SSW2019 was classified as minor warming, the size of the Antarctic ozone area in 2019 was comparable with that in 2002 when there was major warming in late September. Furthermore, the second-smallest ozone hole since 1988 was observed in 2017, even though there was no pronounced SSW (Blunden and Arndt 2018). Considering that levels of ozone depleting substances are decreasing, we chose to use 2017 for comparison with 2019 rather than 2002.

It may be possible to explain the ozone hole area and ozone depletion in 2019 on the basis of quasi-stationary wave amplitudes in August and sea surface temperatures in the tropical Pacific and Indian oceans in June (Milinevsky et al. 2020). Wargan et al. (2020) compared ozone hole areas between 2018 and 2019, finding that the small hole in 2019 resulted from the size and geometry of the polar vortex. Safieddine et al. (2020) found that total-column ozone levels poleward of 45°S in September, October, and November 2019 were 29%, 28%, and 26%, respectively, higher than the previous 11-year average, based on Infrared Atmospheric Sounding Interferometer (IASI) ozone data. It has also been found that the quasi-stationary wave in the late austral winter (August) played a major role in preventing expansion of the 2017 ozone hole (Evtushevsky et al. 2019).

Weber et al. (2003) suggested that ozone hole size is controlled mainly by wave dynamics. The relationship between the vertical component of the E–P flux, averaged over 30°S–90°S at 100 hPa for August, and maximum daily ozone hole areas in the austral spring, 2002–2019, are shown in Figure 5.3, with a correlation coefficient, r , between these variables of -0.62 . This supports a strong linkage between planetary wave activity at middle–high latitudes and Antarctic ozone hole area.

The ozone hole was smaller in 2002, 2017, and 2019 when there was strong wave propagation into the stratosphere. In 2002, the major SSW occurred late in September with the intermittently strong PW 1 and 2 weakening the PNJ prior to the SSW, preventing expansion of the ozone hole (Allen et al. 2003; Baldwin et al. 2003; Newman and Nash 2005). Pronounced planetary wave events in August and September 2017 might have led to low ozone depletion during September–November (Evtushevsky et al. 2019). In 2019 (Section 4), there was pronounced propagation of waves of WN 1 into the stratosphere from late August, resulting in mid-stratospheric temperature increases in polar regions. An anomalously small Antarctic ozone hole thus occurred in 2019.

In contrast, little planetary wave activity may lead to severe ozone depletion. For example, in 2015 there was less wave propagation into the stratosphere during July–October, with below-average temperatures persisting. As a result, the 2015 Antarctic ozone hole was one of the largest since measurements began (Blunden and Arndt 2016).

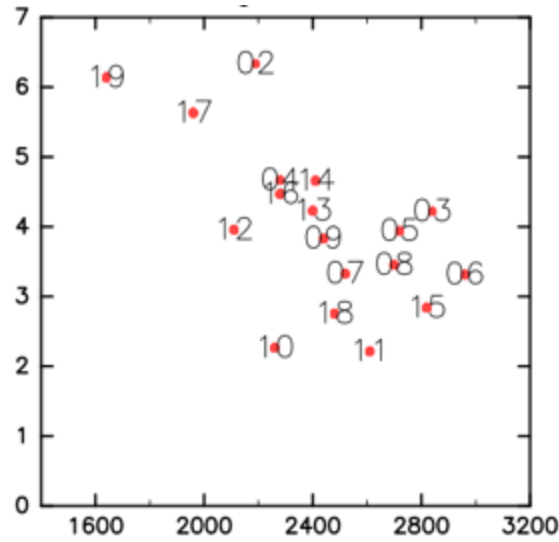


Figure 5.3 Scatterplot of the maximum daily ozone-hole area ($\times 10^4 \text{ km}^2$) in the austral winter/spring (August–November) and the vertical component of the E–P flux averaged over 30°S – 90°S at 100 hPa for August [$\times 10^4 \text{ kg s}^{-2}$]. The numbers refer to different years from 2002 to 2019. Each year is denoted by its last two digits (e.g., 02 means 2002).

The daily evolution of ozone hole area during 2019 is depicted in Figure 5.4. During 2019, the ozone hole expanded from early August to early September, reaching its largest area of $\sim 1.5 \times 10^7 \text{ km}^2$ on 7 September before shrinking rapidly from mid-September to October. The corresponding quantities for 2017 are shown in Figure 5.4 for comparison. In both years, the ozone holes developed normally with growth occurring due to chlorine-based depletion reactions during late August to early September (Newman et al. 2004). This occurred similarly in 2012. Concentrations of ozone-depleting substances (e.g., Cl and Br) in the Antarctic stratosphere were thus still high enough to cause severe ozone depletion (Figure 5.1) (Kramarova et al. 2014).

Compared with the rapid hole shrinkage in September 2019, the hole area decreased at a moderate rate in the second half of September 2017, to an area of $(1.05\text{--}1.75) \times 10^7 \text{ km}^2$ in late September, compared with a mean value of $\sim 2.0 \times 10^7 \text{ km}^2$. Furthermore, in contrast to the smaller area than average in September 2017, in 2019 the hole area remained well below mean climatological values for 1979–2016, at close to the 10th percentile of climatological values, until the end of October. The ozone hole disappeared at the beginning of November 2019, earlier than indicated by climatological records for early December.

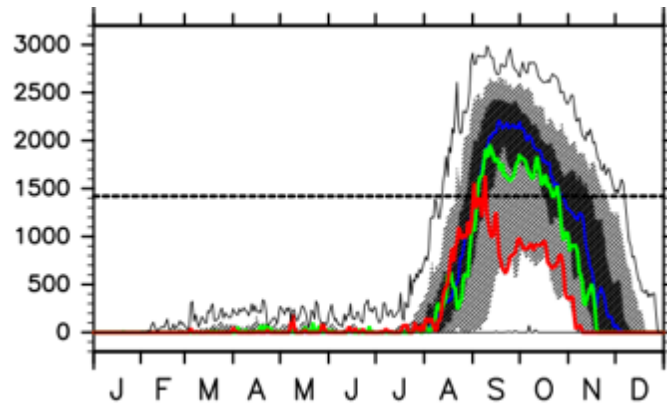


Fig. 5.4 Time series of ozone hole area [$\times 10^4 \text{ km}^2$] defined as the region with ozone concentrations of $<220 \text{ DU}$ south of 40°S . Red and green lines indicate 2019 and 2017, respectively. Blue line represents climatological values for 1979–2016. The lines and shaded areas from bottom to top denote minimum, 10th, 30th, mean, 70th, 90th percentile, and maximum, respectively. The horizontal black line indicates the area of the Antarctic.

An anomalously small and irregularly shaped ozone hole was observed together with a significantly disturbed polar vortex in September 2019. The evolution of OMI total-column ozone distributions in 2017 and 2019 are compared in Figure 5.5 where the gray-shaded region indicates total-column ozone < 220 DU. In late August 2019, before strong wave activities disturbed the vortex, the ozone hole began to form while there was a low total-column ozone region south of South America. A similar ozone hole region appeared southeast of South America in late August 2017. This hole changed after September; while the 2017 hole covered most of the Antarctic, the 2019 hole shifted off the South Pole to be relocated near the edge of the Antarctic on 7 September when it reached its maximum area with an irregular shape (compared with that during 2017). In addition, a pronounced high-ozone “collar” region appeared over the 30°S – 60°S region in September 2019 (Figure 5.5). A comparison of the 2019 ozone hole with a typical Antarctic ozone hole was undertaken by Wargan et al. (2020) using the Global Earth Observing System Constituent Data Assimilation System (GEOS). The South Pole was located within the ozone holes in October in both 2017 and 2019, although it was near the edge of the hole in 2019.

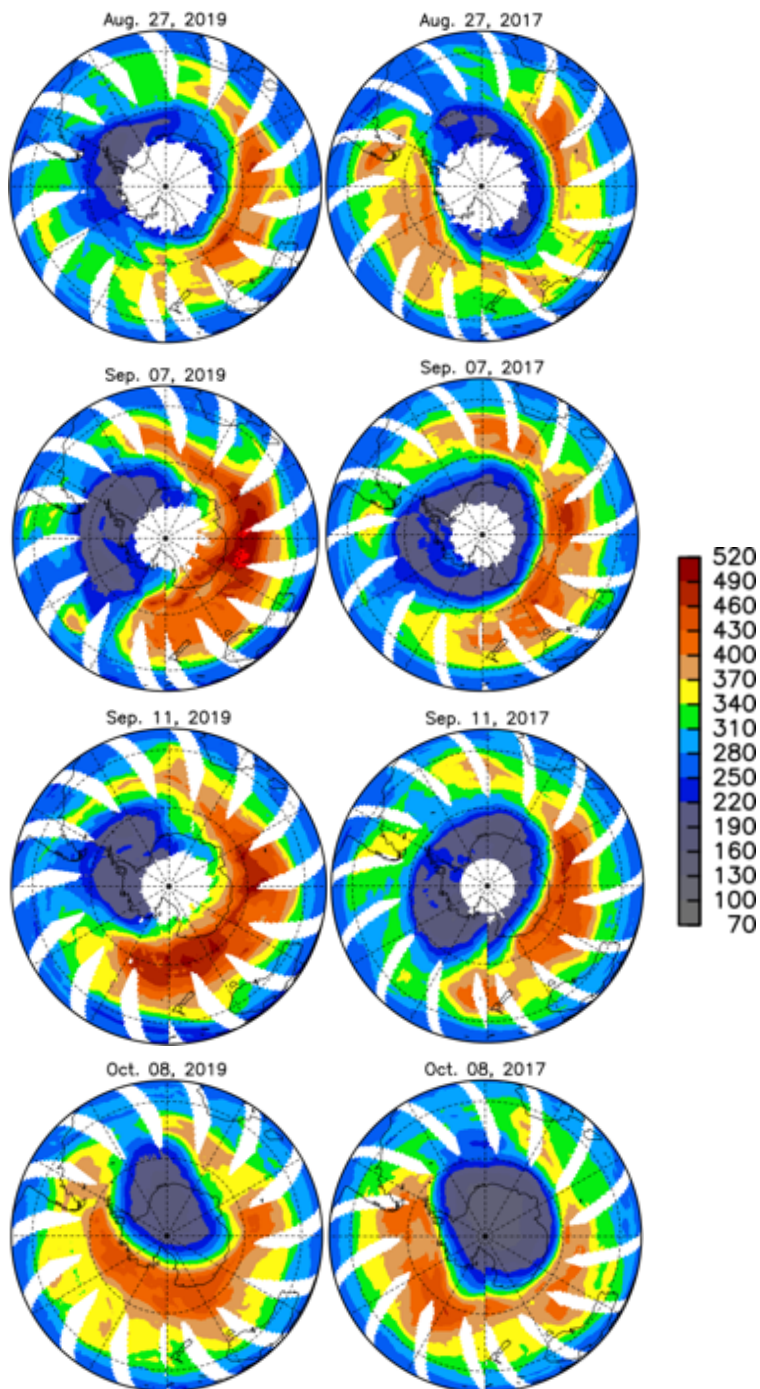


Figure 5.5 Daily mean total-column ozone (DU) from the satellite OMI instrument for 27 August, 7 September, 11 September, and 8 October in 2019 (left) and 2017 (right). The contour interval is 30 DU. White areas indicate missing data during polar night.

Temperatures in the lower stratosphere around the polar ice-cap were higher than average during the late austral winter in both 2017 and 2019. Figure 5.6 shows temperature evolution around the polar cap averaged from 60°S to 90°S. Ozone destruction occurs in the lower stratosphere, and the red and green lines (Figure 5.6) indicate daily temperatures at 50 hPa averaged over the region south of 60°S; the blue line indicates climatological values. In 2019, temperatures were near average until the beginning of August, began to rise in mid-August, and continued to rise through mid-September with higher than average temperatures persisting until mid-November. In 2017, temperatures were near average until early August, increasing from mid-August through early September, preventing PSC formation in the lower stratosphere.

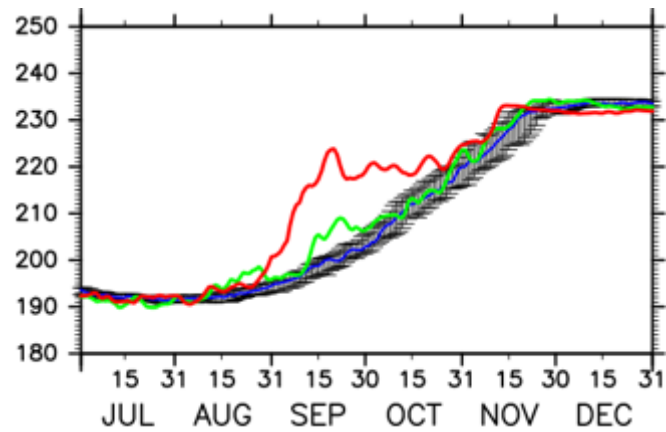


Fig. 5.6 Time series of temperature (K) averaged over the region 60°S–90°S at 50 hPa. Green and red lines indicate 2017 and 2019, respectively. Mean values for 1979–2016 are indicated by the blue line. The error bar denotes the 30th and 70th percentile values of the mean over the period 1979–2016. Data provided by NASA.

The above-average amount of ozone mid-stratosphere indicates reduced depletion during late winter and early spring in 2017 and 2019. Deviations from climatological zonal-mean volume mixing ratios averaged over 60°S–80°S during 2017 and 2019 are shown in Figure 5.7. In 2019, a marked increase in ozone level occurred from the end of August through the first half of October at 50–10 hPa where ozone depletion usually occurs. In 2017, a significant increase in mixing ratio occurred during mid-August and mid-September. The evolution of the zonal-mean volume-mixing-ratio anomaly corresponds to the development of the ozone hole (Figure 5.4). August and early September are periods when chlorine compounds exert their main effects on the ozone hole area (Newman et al. 2004), with the hole being strongly impacted by wave dynamics and its influence on temperature (Weber et al. 2003). In the 2019 case (Section 4), the SSW2019 event resulted from wave dynamics during late August to September when depletion reactions occurred, limiting expansion of the ozone hole. Evtushesky et al. (2019) suggested that the reduced ozone depletion in the spring of 2017 might have been due to significant wave dynamics during late winter.

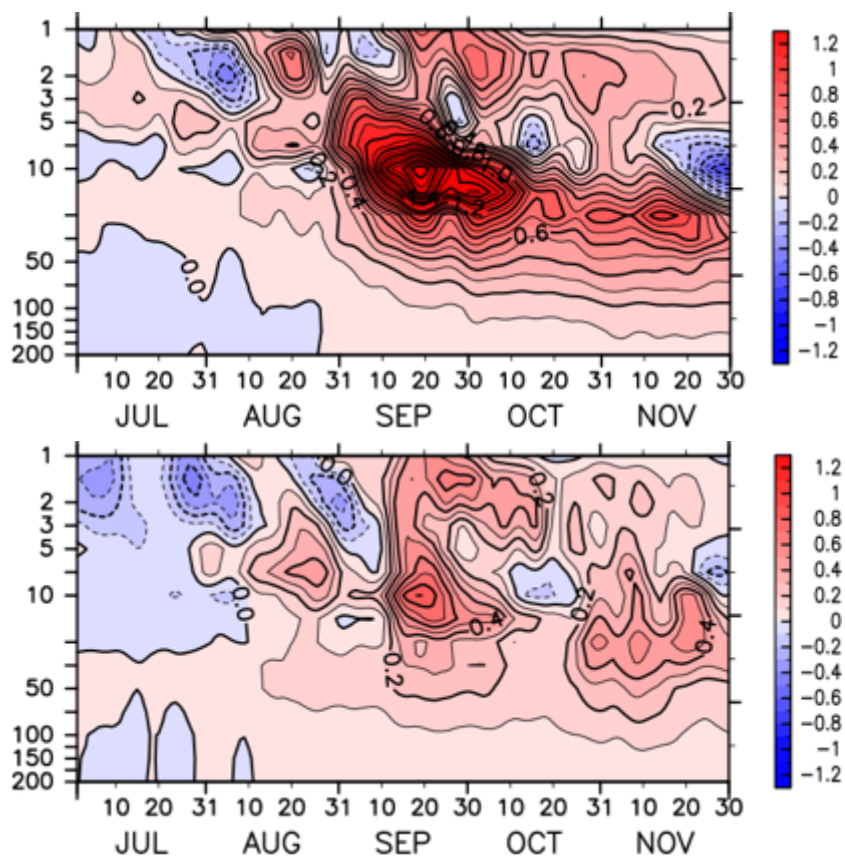


Figure 5.7 Time–height cross sections of deviations of zonal-mean ozone volume mixing ratios (ppmv) averaged over 60°S to 80°S for 2019 (top) and 2017 (bottom) from 1 July to 30 November. The contour interval is 0.1 ppmv.

The evolution of wave amplitudes and EPFz in 2019 is described in Figure 4.4 and that for 2017 here in Figure 5.8, which shows daily changes of wave amplitudes of Z1 and 2 (geopotential height waves of PW1 and 2) at 60°S and 10 hPa (top) and 50 hPa upward E–P fluxes of zonal PW from 1 to 3 (bottom) in 2017.

The larger amplitude of Z1 on 1 August 2017 (~1239 m) was followed by its largest amplitude on 18 August 2017 (~1395 m). Several large Z1 amplitudes occurred in September and early October. Similar variations in daily amplitudes of waves 1 and 2 at 50 hPa were reported from ERA-Interim reanalysis (Klekociuk et al. 2019). Such large amplifications of PW1 disturb the polar vortex, leading to reduction of the PNJ. In contrast to the predominant role of PW1 in August and September 2019, WN 2 played a role in mid-August and mid-September in 2017.

The Hovmöller diagram (Figure 4.5) indicates dominant wave modes in 2019 and 2002. In 2019 (Section 4) Z1 became dominant over Z2 from ~10 August to ~20 September. Figure 5.9 repeats the analysis for 2017, indicating that Z2 regularly travelled eastward in mid-August and mid-September in 2017 with a period of ~10 days. The amplitudes of Z1 and Z2 strengthened during mid-September but did not lead to an SSW event. The Z2 eastward-travelling waves occurring in the SH stratospheric winter (Shiotani et al. 1993) and their wave–wave interactions with quasi-stationary WN 1 contribute to weakening of the PNJ (Krüger et al. 2005).

The daily evolution of total EPFz at 50 hPa for all three wavenumbers in 2017 is shown by gray shading in Figure 5.8 (bottom), together with the EPFz values of PW 1–3 (colored lines). Evtushevsky et al. (2019) found that the development of large amplitude stratospheric planetary waves at high southern latitudes during August 2017 was comparable with that for the same month in years with smaller ozone holes (2002 and 1988). To gauge the disturbance within the vortex in the lower stratosphere, we investigated wave propagation by examination of EPFz at 50 hPa. The largest upward propagation occurred on 13 September 2017. The total EPFz in 2017 indicates active planetary wave propagation to the stratosphere, peaking mid-September, corresponding to increasing temperatures at the polar ice cap (Figure 5.5). The contribution of the zonal WN 1 component is considerably greater than that of other wavenumber components in 2019, whereas in 2017, WN 2 played a role in mid-September. Furthermore, PW1–3 display simultaneous peaks, leading to the largest wave activity on 13 September. The maximum value of total EPFz in 2017 ($\sim 51 \times 10^4 \text{ kg s}^{-2}$) exceeded that of 2019 ($\sim 45 \times 10^4 \text{ kg s}^{-2}$). The SSW2019 event was thus characterized by growth of PW1 wave activity, which disturbed the polar vortex before and during the warming period.

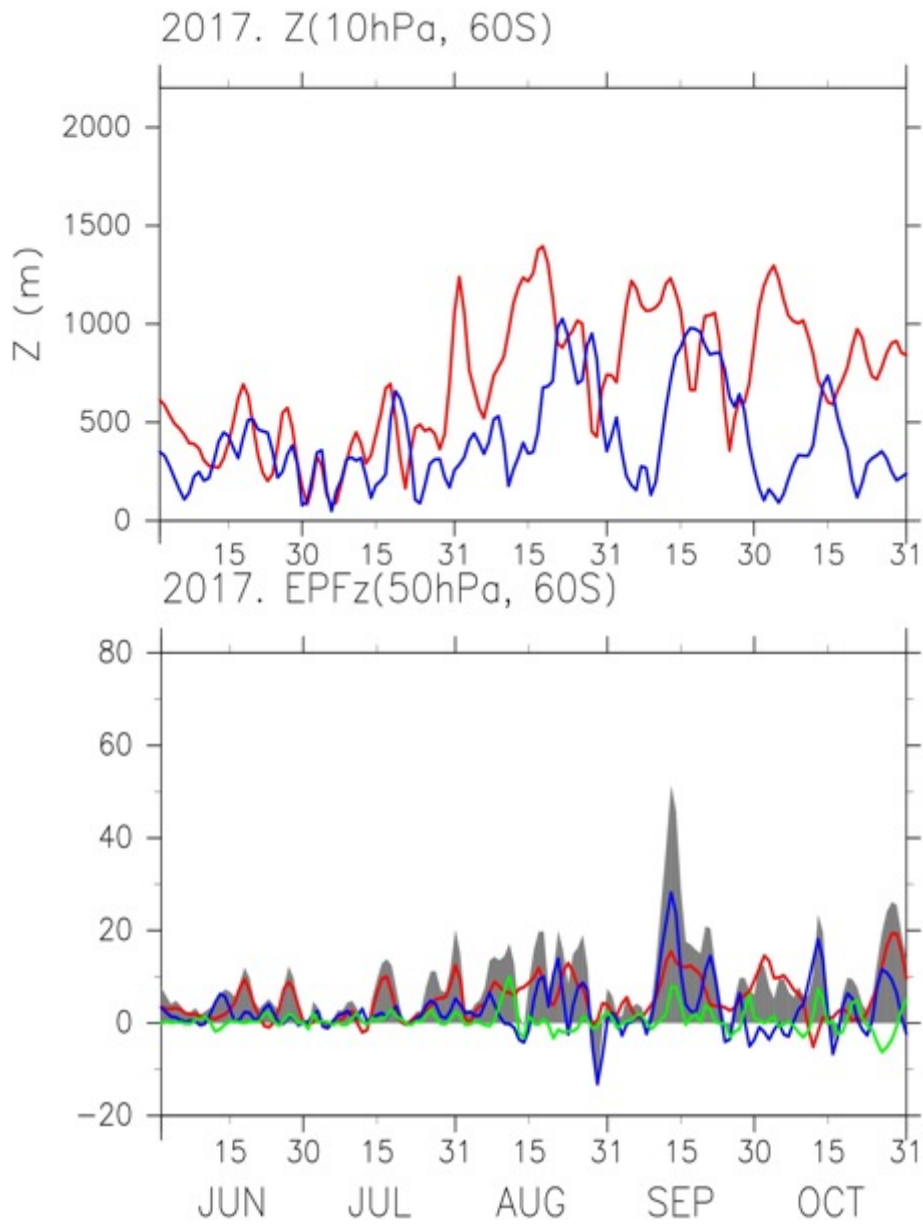


Figure 5.8 Figure 4.4 repeated for 2017.

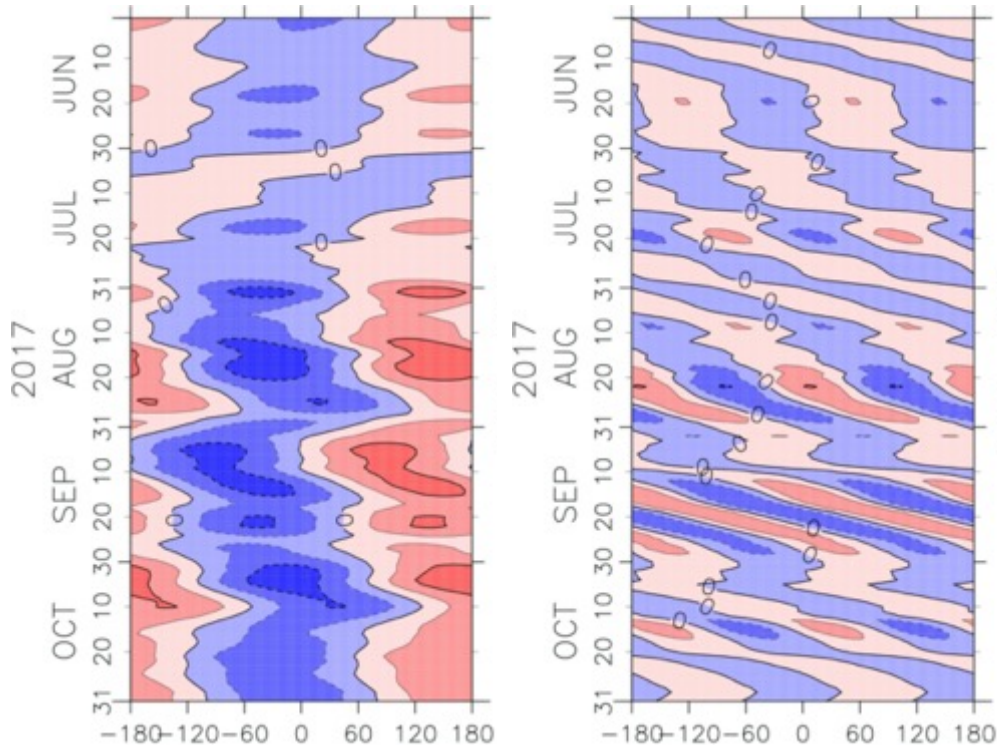


Figure 5.9. Figure 4.5 repeated for 2017.

The evolution of vertical component of the residual mean circulation (\bar{w}^*) was studied as an indicator of the strength of residual mean circulation, with the time evolution of residual vertical velocities (averaged over 60°S–80°S) at 10 hPa, an ozone-rich altitude, in 2017 and 2019 being shown in Figure 5.10. In 2019, downward motion varied intermittently throughout late August to mid-September, with at least three periods of significant downward motion. Intermittently strong planetary waves in the stratosphere resulted in strong downward motion, possibly leading to ozone transport into the vortex as discussed in Section 2. Brewer–Dobson circulation is driven by planetary wave breaking, as indicated by stratospheric E–P flux divergence, with ozone at high latitudes being transported from the upper stratosphere by the strong downwelling. In 2017, residual vertical velocities fluctuated from August through September, with significant downwelling occurring around 20 September.

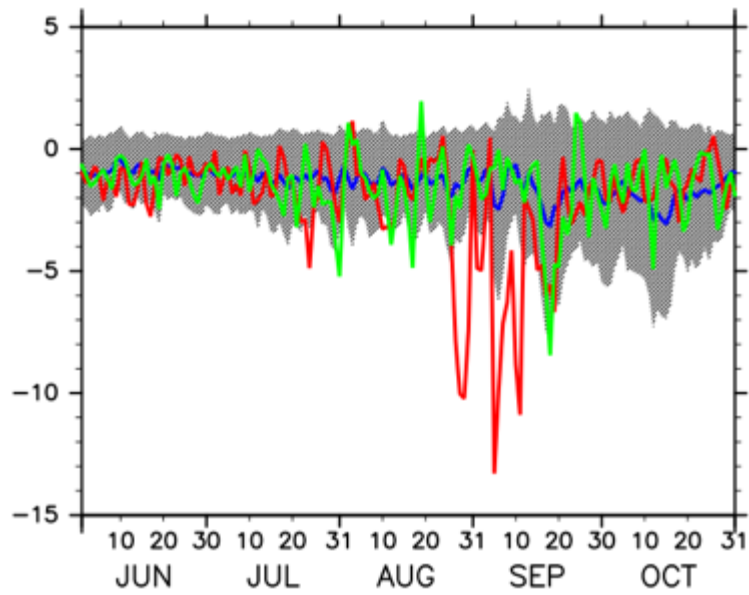


Figure 5.10 Time series of the residual vertical velocities averaged over 60°S to 80°S at 10 hPa. Green and red lines indicate 2017 and 2019, respectively. The blue line indicates mean climatological values for 2005–2019 with standard deviation (shaded).

Trends in ozone concentrations were considered rather than zonal mixing because the trend in zonal-mean ozone mixing ratio is correlated with variations in large-scale circulation (Eq. 2.22). Trends in zonal-mean ozone volume mixing ratio (the term on left in Eq. 2.22) in 2017 and 2019 are shown in Figure 5.11. Ozone concentrations increased significantly from late August to mid-September 2019 at 50–10 hPa. Major wave-activity events and warming were observed in the SH during the 2019SSW (Figures 4.3 and 4.4). Ozone concentrations decreased during 20–30 September but were still higher than climatological values noted in Figure 5.7. In 2017, ozone levels increased mid-September at 20–5 hPa when strong planetary wave activity occurred in the lower stratosphere (Figure 5.8). Furthermore, an increasing ozone trend also occurred mid-August at 20–5 hPa, corresponding to large wave amplitudes of mid-August.

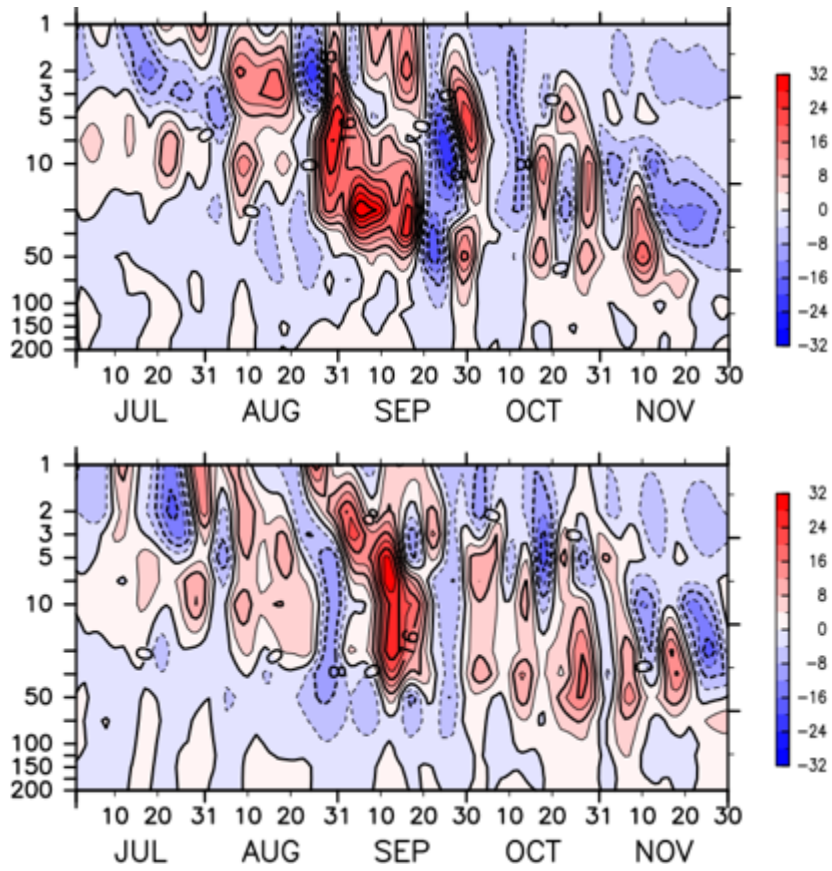


Figure 5.11 Time–height cross sections of trends in zonal-mean ozone volume mixing ratios averaged over 60°S to 80°S for 2019 (top) and 2017 (bottom), July to November. The contour interval is 4×10^{-8} ppmv day⁻¹.

Vertical transport and ozone concentrations are compared in Figure. 5.11, while Figure 5.12 indicates ozone transport in terms of residual vertical velocity (second term on right in Eq. 2.22). In 2019, there was increasing ozone transport by residual vertical transport at 50–10 hPa from late August to mid-September, when intermittently strong downwelling at 10 hPa was associated with increasing ozone concentrations (Figures 5.10 and 5.11). In 2017, the ozone concentration increased due to vertical transport mid-September, with strong downwelling occurring at 10 hPa at ~20 September. Ozone levels increased due to vertical transport at 20–10 hPa, corresponding to an increasing ozone trend during 10 August to late August at 20–5 hPa. In both 2017 and 2019, there was increasing vertical transport in October and November, consistent with increasing ozone levels (Figure 5.11).

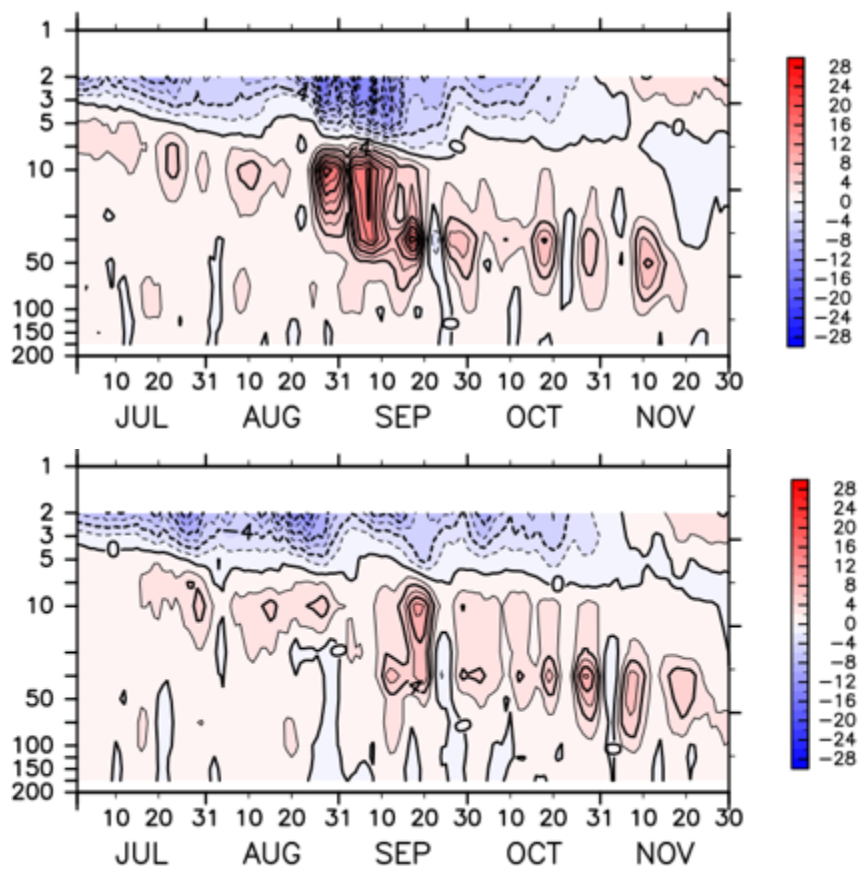


Figure 5.12 Time–height cross sections of zonal-mean ozone volume mixing ratio and residual vertical velocities averaged over 60°S to 80°S for 2019 (top) and 2017 (bottom), July–November. The contour interval is 2×10^{-8} ppmv day⁻¹.

6. Conclusions

The evolution of the SSW2019 event in the SH was analyzed using the JRA-55 dataset in comparison with the major warming event of 2002 (Section 4). The relationship of the Antarctic ozone hole in 2017 and 2019 with dynamical fields was also studied (Section 5).

Unusual warming and weakened westerly winds occurred at high latitudes in the SH in September 2019. However, since reversal of westerly winds to easterly winds was not observed at 60°S, 10 hPa, SSW2019 was classified as a minor SSW event on the basis of World Meteorological Organization criteria.

Pronounced temperature increases occurred during early September 2019, following two sudden warming events in late August. Stratospheric temperatures at the South Pole were well above plus one standard deviation of the mean during most of September. During 2019, westerly winds weakened in the stratosphere from late August. A reversal of zonal-mean zonal winds from westerly to easterly occurred in the upper stratosphere in early September, but did not reach the 10 hPa level. The PNJ weakened considerably during the warming period.

This study has shown that the amplification of quasi-stationary PW1 was pronounced in SSW2019. Propagation of the planetary wave to the stratosphere was investigated by study of the vertical component of the E–P flux. Waveguide analysis has shown that, during the warming period, planetary waves propagated upward to the stratosphere

through a high-latitude waveguide. The sustained occurrence of the waveguide allowed upward propagating planetary waves to cause weakening of the PNJ until late September. Strong and persisting quasi-stationary PW1 planetary waves thus propagated to the stratosphere during the warming period. The quasi-stationary PW1 thus played a dominant role in the SSW2019, unlike the regular occurrence of eastward-traveling PW2 in the SSW2002 event.

Study of interannual changes in the wave forcing in September has shown that the total wave forcing and PW1 of 2019 were the highest for 2002–2019.

The occurrence of preconditions prior to major warming in SSW2002 has been widely reported, but they were largely absent in the SSW2019 event, perhaps explaining the lack of the reversal of zonal-mean zonal winds at or below 10 hPa during that event. Although SSW2019 does not meet WMO criteria for a major SSW event, the large increase in temperature at high latitudes had a significant impact on the stratosphere with, for example, the formation of the Antarctic ozone hole in the austral spring. As an ozone-depletion diagnostic, the Antarctic 2019 ozone-hole area was the smallest since 1988.

Ozone volume-mixing-ratio data from the MLS aboard the Aura satellite and JRA-55 data were used to analyze dynamical features of ozone hole changes in 2019 and for comparison with those of 2017, with both years having small ozone holes.

Severe ozone depletion has been observed in the Antarctic since the 1980s. Rapid ozone depletion is caused largely by heterogeneous chemical reactions, primarily with

chlorine- and bromine-containing compounds. The Antarctic ozone-hole area varies from year to year, due mainly to dynamical effects. The 2019 ozone hole was one of the smallest since 1988, with a maximum daily hole size of 16.4 million km². Development of the hole began in early August, with the hole area then decreasing in late September, and disappearing rapidly on 9 November (based on comparison with average early-December data). This ozone reduction resulted from the unusually large dynamical effect of the stratospheric polar vortex in September, due to the occurrence of SSW2019. In 2017, the hole again began expanding in early August, peaking on 11 September and disappearing by 19 November.

Our results indicate an apparent zonal-mean ozone-volume-mixing-ratio anomaly at 50–10 hPa from late August to September and mid-September in 2019 and 2017. This is consistent with the small ozone hole areas of those years. Significantly large and dominant wave activities of zonal WN 1 occurred in late August and September 2019, while eastward-travelling WN 2 waves and WN 1 and 3 waves occurred in mid-September 2017. Intermittent upsurges of wave activity occurred during the austral winter in the mid-stratosphere. Downward motion was enhanced in both years, in association with the strong wave activities. This caused the downward advection of ozone-rich air, leading to the small hole size in both years. Trends in zonal-mean ozone mixing ratio are consistent with residual vertical transport during the increasing-ozone period.

Dynamical features of the SH SSW2019 event were compared with those of the SSW2002 event (Section 4). SSWs rarely occur in the SH, so comparison with major NH SSWs were necessary to explain the minor status of SSW2019 (Section 5). Ozone transport by vertical residual mean meridional circulation is analyzed qualitatively (Section 5), but further quantitative analysis is necessary. Further study of ozone variations due to photochemical processes is also required, together with comparisons of different reanalysis datasets.

Acknowledgements

I sincerely thank my supervisor, Prof. Toshihiko Hirooka, Department of Earth and Planetary Science, Kyushu University, Japan for his guidance and assistance, without which I would never have completed this study.

I also acknowledge my dissertation committee members, Prof. Ryuichi Kawamura, Department of Earth and Planetary Science, Kyushu University; Dr Nawo Eguchi, Research Institute for Applied Mechanics, Kyushu University; and Dr Hideharu Akiyoshi, National Institute for Environment Studies for their helpful suggestions. I also like thank Prof. Kirstin Krüger, University of Oslo, Norway, for helpful discussion and comments.

I am grateful to the laboratory staff of Atmospheric and Geophysical Fluid Dynamics. I thank other faculty members, researchers, graduate students, and staff of the Department of Earth and Planetary Sciences, Kyushu University.

Finally, I thank my parents for their endless love, support, and encouragement; and all scholarship supporters throughout the course of my study in Japan.

Data Availability Statements

The JRA-55 data set used in this paper is available on the JMA Data Dissemination System (https://jra.kishou.go.jp/JRA-55/index_en.html). The Aura MLS science teams provided high-quality satellite ozone data; MLS data are available from the NASA Goddard Space Flight Center Earth Science Data and Information Services Center (GES-DISC, <https://disc.gsfc.nasa.gov/>). Ozone maps and other meteorological data related to ozone may be found at <https://ozonewatch.gsfc.nasa.gov/>.

The GFD-DENNOU Library was used for graphical output.

References

- Allen, D. R., R. M. Bevilacqua, G. E. Nedoluha, C. E. Randall, and G. L. Manney, 2003. Unusual Stratospheric Transport and Mixing during the 2002 Antarctic Winter. *Geophysical Research Letters*, 30, 1599, doi:10.1029/2003GL017117.
- Andrews, D. G. and M. E. McIntyre, 1976. Planetary Waves in Horizontal and Vertical Shear: The Generalized Eliassen-Palm Relation and the Mean Zonal Acceleration. *Journal of Atmospheric Sciences* 33(11), 2031–2048.
- Andrews, D. G., J. R. Holton, and C. B. Leovy, 1987. *Middle Atmosphere Dynamics*, (p. 489). Orland, Academic press.
- Baldwin, M. P., T. Hirooka, A. O'Neill, S. Yoden, A. J. Charlton, Y. Hio, W. A. Lahoz, and A. Mor, 2003. Major Stratospheric Warming in the Southern Hemisphere in 2002: Dynamical Aspects of the Ozone Hole Split. *SPARC Newsletter*, No. 20, SPARC Office, Toronto, ON, Canada, 24–26.
- Blunden, Jessica and Derek S. Arndt. 2016. State of the Climate in 2015. *Bulletin of the American Meteorological Society* 97(8), Si--S275.
- Blunden, J. and D. S. Arndt, 2018. State of the Climate in 2017. *Bulletin of the American Meteorological Society* 99(8):Si--S310.
- Brasseur, G. P. and S. Solomon. 2005, Dynamics and Transport. *Aeronomy of the Middle Atmosphere: Chemistry and Physics of the Stratosphere and Mesosphere* 51–149.

- Butler, A. H., J. P. Sjoberg, D. J. Seidel, and K. H. Rosenlof, 2017. A Sudden Stratospheric Warming Compendium. *Earth System Science Data* 9(1), 63–76.
- Charlton, A. J. and L. M. Polvani, 2007. A New Look at Stratospheric Sudden Warmings. Part I: Climatology and Modeling Benchmarks. *Journal of Climate* 20(3), 449–469.
- Charney, J. G. and P. G. Drazin, 1961. Propagation of planetary-scale disturbances from the lower into the upper atmosphere, *Journal of Geophysical Research*: 83-109.
- Chubachi, S., 1984. Preliminary results of ozone observations at Syowa Station from February 1982 to January 1983, Memoir National Institute of Polar Research, Special Issue, 34, 13–19.
- Dickinson, R. E., 1968. Planetary Rossby Waves Propagating Vertically through Weak Westerly Wind Wave Guides. *Journal of Atmospheric Sciences* 25(6), 984–1002.
- Edmon Jr, H. J., Hoskins, B. J., McIntyre, M. E., 1980. Eliassen-Palm cross sections for the troposphere. *Journal of Atmospheric Sciences*, 37(12), 2600-2616.
- Eliassen, A., 1960. On the Transfer of Energy in Stationary Mountain Waves. *Geophysical Publications* 22, 1–23.
- Eswaraiah, S., J-H. Kim, W. Lee, J. Hwang, K. Kumar, and Y. Kim, 2020. Unusual Changes in the Antarctic Middle Atmosphere during the 2019 Warming in the Southern Hemisphere. *Geophysical Research Letters* 47(19), :e2020GL089199.

- Evtushevsky, O., A. R. Klekociuk, V. Kravchenko, G. Milinevsky, and A. Grytsai, 2019. The Influence of Large Amplitude Planetary Waves on the Antarctic Ozone Hole of Austral Spring 2017. *Journal of Southern Hemisphere Earth Systems Science* 69(1), 57–64.
- Farman, J. C., B. G. Gardiner, and J. D. Shanklin, 1985. Large Losses of Total Ozone in Antarctica Reveal Seasonal ClO_x/NO_x Interaction. *Nature* 315(6016), 207–210.
- Harada, Y. and T. Hirooka, 2017. Extraordinary Features of the Planetary Wave Propagation during the Boreal Winter 2013/2014 and the Zonal Wave Number Two Predominance. *Journal of Geophysical Research: Atmospheres* 122(21), 11–374.
- Iida, C., T. Hirooka, and N. Eguchi, 2014. Circulation Changes in the Stratosphere and Mesosphere during the Stratospheric Sudden Warming Event in January 2009. *Journal of Geophysical Research* 119(12), 7104–7115.
- Julian, P. R. 1967. Midwinter Stratospheric Warmings in the Southern Hemisphere General Remarks and a Case Study. *Journal of Applied Meteorology and Climatology* 6(3), 557–563.
- Klekociuk, A. R., M. B. Tully, P. B. Krummel, O. Evtushevsky, V. Kravchenko, S. I. Henderson, S. P. Alexander, R. R. Querel, S. Nichol, D. Smale, G. P. Milinevsky, A. Grytsai, P. J. Fraser, Z. Xiangdong, H. Peter Gies, R. Schofield and J. D.

- Shanklin, 2019. The Antarctic Ozone Hole during 2017. *Journal of Southern Hemisphere Earth Systems Science* 69(1), 29–51.
- Kobayashi, S., Y. Ota, Y. Harada, A. Ebata, M. Moriya, H. Onoda, K. Onogi, H. Kamahori, C. Kobayashi, H. Endo, K. Miyaoka, and T. Kiyotoshi, 2015. The JRA-55 Reanalysis: General Specifications and Basic Characteristics. *Journal of the Meteorological Society of Japan* 93(1), 5–48.
- Komhyr, W. D., R. D. Grass, and R. K. Leonard, 1986. Total Ozone Decrease at South Pole, Antarctica, 1964–1985. *Geophysical Research Letters* 13(12), 1248–1251.
- Kramarova, N. A., E. R. Nash, P. A. Newman, P. K. Bhartia, R. D. McPeters, D. F. Rault, C. J. Seftor, P. Q. Xu, and G. J. Labow, 2014. Measuring the Antarctic Ozone Hole with the New Ozone Mapping and Profiler Suite (OMPS). *Atmospheric Chemistry and Physics* 14(5), 2353–2361.
- Krüger, K., B. Naujokat, and K. Labitzke, 2005. The Unusual Midwinter Warming in the Southern Hemisphere Stratosphere 2002: A Comparison to Northern Hemisphere Phenomena. *Journal of Atmospheric Sciences* 62(3) 603–613.
- Labitzke, K. 1968. Midwinter Warmings in the Stratosphere and Lower Mesosphere (Rocket and Radiosondes Data from Measurements over Northern Hemisphere Used to Study Stratospheric and Mesospheric Circulation during Three Midwinter Periods). *Zeitschrift für Geophysik* 34(6), 555–561.

- Labitzke, K., 1981. The Amplification of Height Wave 1 in January 1979: A Characteristic Precondition for the Major Warming in February. *Monthly Weather Review* 109(5), 983–989.
- Levelt, P. F., E. Hilsenrath, G. W. Leppelmeier, G. H. J. van den Oord, P. K. Bhartia, J. Tamminen, J. F. de Haan, and J. P. Veefkind, 2006. Science Objectives of the Ozone Monitoring Instrument. *IEEE Transactions on Geoscience and Remote Sensing* 44(5), 1199–1208.
- Levelt, P. F., G. H. J. Van Den Oord, M. R. Dobber, A. Malkki, H. Visser, J. De Vries, P. Stammes, J. O. V. Lundell, and H. Saari, 2006. The Ozone Monitoring Instrument. *IEEE Transactions on Geoscience and Remote Sensing* 44(5), 1093–1101.
- Lim, E., H. H. Hendon, A. H. Butler, R. D. Garreaud, I. Polichtchouk, T. G. Shepherd, A. Scaife, R. Comer, L. Coy, P. A. Newman, D. W. J. Thompson, H. Nakamura, 2020. The 2019 Antarctic Sudden Stratospheric Warming. *SPARC Newsletter*. 54, 10–13.
- Livesey, N. J., W. G. Read, P. A. Wagner, L. Froidevaux, A. Lambert, G. L. Manney, L. F. Millán Valle, H. C. Pumphrey, M. L. Santee, M. J. Schwartz, A. Lambert, L. F. M. Valle, H. C. Pumphrey, G. L. Manney, R. A. Fuller, R. F. Jarnot, B. W. Knosp, R. R. Lay, 2018. *Version 4.2 x Level 2 Data Quality and Description Document, Jet Propulsion Laboratory*.

- Matsuno, T.. 1971, A Dynamical Model of the Stratospheric Sudden Warming. *Journal of Atmospheric Sciences* 28(8), 1479–1494.
- Milnevsky, G., O. Evtushevsky, A. Klekociuk, Y. Wang, A. Grytsai, V. Shulga, and O. Ivaniha, 2020. Early Indications of Anomalous Behaviour in the 2019 Spring Ozone Hole over Antarctica. *International Journal of Remote Sensing* 41(19), 7530–7540.
- Newman, P. A., S. R. Kawa, and E. R. Nash, 2004. On the Size of the Antarctic Ozone Hole. *Geophysical Research Letters* 31(21).
- Newman, P. A. and E. R. Nash, 2005. The Unusual Southern Hemisphere Stratosphere Winter of 2002. *Journal of Atmospheric Sciences* 62(3), 614–628.
- Plumb, R. Alan, 2002. Stratospheric Transport. *Journal of the Meteorological Society of Japan. Ser. II* 80(4B), 793–809.
- Rao, J., C. I. Garfinkel, I. P. White, and C. Schwartz. 2020. The Southern Hemisphere Minor Sudden Stratospheric Warming in September 2019 and Its Predictions in S2S Models. *Journal of Geophysical Research: Atmospheres* 125(14), 1–19.
- Safieddine, S., M. Bouillon, A. C. Paracho, J. Jumelet, F. Tencé, A. Pazmino, F. Goutail, C. Wespes, S. Bekki, A. Boynard, J. Hadji-Lazaro, P. François Coheur, D. Hurtmans, and C. Clerbaux, 2020. Antarctic Ozone Enhancement During the 2019 Sudden Stratospheric Warming Event. *Geophysical Research Letters* 47(14), 1–10.

- Salby, M. L., E. A. Titova, and L. Deschamps, 2012. Changes of the Antarctic Ozone Hole: Controlling Mechanisms, Seasonal Predictability, and Evolution. *Journal of Geophysical Research: Atmospheres* 117(D10).
- Scherhag, R., 1952. Die Explosionartigen Stratosphärenwärmungen Des Spätwinters 1951-1952. *Ber. Deut. Wetterd.*, 6, 51–63.
- Shiotani, M., N. Shimoda, and I. Hirota, 1993. Interannual Variability of the Stratospheric Circulation in the Southern Hemisphere. *Quarterly Journal of the Royal Meteorological Society* 119(511), 531–546.
- Solomon, S., 1999. Stratospheric Ozone Depletion: A Review of Concepts and History. *Reviews of Geophysics* 37(3), 275–316.
- Solomon, S., D. J. Ivy, D. Kinnison, M. J. Mills, R. R. Neely, and A. Schmidt, 2016. Emergence of Healing in the Antarctic Ozone Layer. *Science* 353(6296), 269–274.
- Stolarski, R. S., A. J. Krueger, M. R. Schoeberl, R. D. McPeters, P. A. Newman, and J. C. Alpert, 1986. Nimbus 7 Satellite Measurements of the Springtime Antarctic Ozone Decrease. *Nature* 322(6082), 808–811.
- Stolarski, R. S., R. D. McPeters, and P. A. Newman, 2005. The Ozone Hole of 2002 as Measured by TOMS. *Journal of Atmospheric Sciences* 62(3), 716–720.
- Wargan, K., B. Weir, G. L. Manney, S. E. Cohn, and N. J. Livesey, 2020. The Anomalous 2019 Antarctic Ozone Hole in the GEOS Constituent Data

Assimilation System with MLS Observations. *Journal of Geophysical Research: Atmospheres* 125(18), e2020JD033335, <https://doi.org/10.1029/2020JD033335>

Waters, J. W., L. Froidevaux, R. S. Harwood, R. F. Jarnot, H. M. Pickett, W. G. Read, P. H. Siegel, R. E. Cofield, M. J. Filipiak, D. A. Flower, J. R. Holden, G. K. Lau, N. J. Livesey, G. L. Manney, H. C. Pumphrey, M. L. Santee, D. L. Wu, D. T. Cuddy, R. R. Lay, M. S. Loo, V. S. Perun, M. J. Schwartz, P. C. Stek, R. P. Thurstans, M. A. Boyles, K. M. Chandra, M. C. Chavez, G.-S. Chen, B. V. Chudasama, R. Dodge, R. A. Fuller, M. A. Girard, J. H. Jiang, Y. Jiang, B. W. Knosp, R. C. LaBelle, J. C. Lam, K. A. Lee, D. Miller, J. E. Oswald, N. C. Patel, D. M. Pukala, O. Quintero, D. M. Scaff, W. V. Snyder, M. C. Tope, P. A. Wagner, and M. J. Walch, 2006. The Earth Observing System Microwave Limb Sounder (EOS MLS) on the Aura Satellite. *IEEE Transactions on Geoscience and Remote Sensing* 44(5), 1075–1092.

Weber, M., S. Dhomse, F. Wittrock, A. Richter, B. M. Sinnhuber, and J. P. Burrows, 2003. Dynamical Control of NH and SH Winter/Spring Total Ozone from GOME Observations in 1995–2002. *Geophysical Research Letters* 30(11), 1583, doi:10.1029/2002GL016799.

Yamazaki, Y., V. Matthias, Y. Miyoshi, C. Stolle, T. Siddiqui, G. Kervalishvili, J. Laštovička, M. Kozubek, W. Ward, D. R. Themens, S. Kristoffersen, and P. Alken, 2020. September 2019 Antarctic Sudden Stratospheric Warming: Quasi-6-Day

Wave Burst and Ionospheric Effects. *Geophysical Research Letters* 47(1),
e2019GL086577. <https://doi.org/10.1029/2019GL086577>.

Julian, P. R., 1967. Midwinter Stratospheric Warmings in the Southern Hemisphere
General Remarks and a Case Study. *Journal of Applied Meteorology and
Climatology*, 6(3), 557–563.

WMO WDCGG DATA SUMMARY No.44 GAW DATA Volume IV-Greenhouse and
Related Gases, November 2020.

Supplementary information

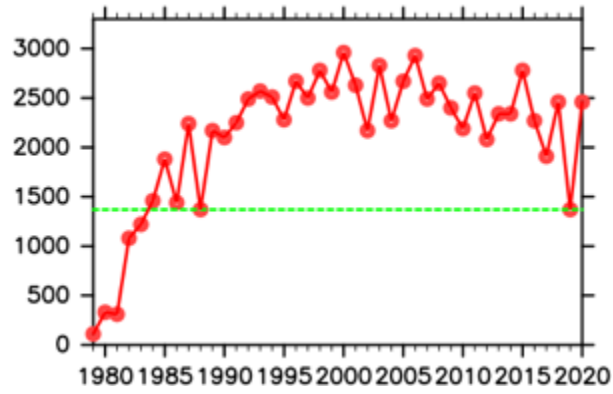


Figure 1S. Same as Figure 5.2, but using data provided by JMA.